Università degli Studi di Padova

Dipartimento di Fisica e Astronomia "G. Galilei"
Master Degree in Astrophysics and Cosmology

FINAL DISSERTATION

The evolution of the night sky spectrum in Asiago

Candidate:
Marco Codato
Badge number 2023377

Supervisor:
Prof. Sergio Ortolani

Co-supervisor:
Prof. Stefano Ciroi

Academic Year 2021 – 2022

Abstract

In this work I analyze the spectral evolution of the night sky at the Asiago Observatory between 2006 and 2021. I developed an automatic pipeline to extract and analyze the background data from spectroscopic observation of astronomical objects. Sky spectra from Asiago are dominated by different artificial sources, which were studied in detail in this work. I conclude that between 2006 and 2021 mercury vapor lamps got reduced by 88%, sodium ones by 67%. Between 2016 and 2021 emission from LED lamps increased by 207%. LED lamps continuum pollutes the blue band of the visible spectrum – previously untouched by artificial emission – and replaces HPS emission in the green-red bands, thus polluting the whole visible spectrum.

Contents

Chapter 1

Introduction

1.1   Introduction to the sky background

In observational ground-based astrophysics the quality of the sky background is one of the most important environmental aspects that can affect the quality of the observations, aside the atmospheric turbulence, which is the other crucial aspect. The most impacting result of a bright sky in astronomical observations is the decrease of the limiting observing magnitude, making fainter objects inaccessible.

There are different natural phenomena that produce diffuse photons backgrounds. Limiting to the optical bands, the most relevant ones are the airglow emission, the zodiacal light and the diffuse galactic emission. Also atmospheric scattering affects the total luminosity of the sky. All of these phenomena and other minor ones are discussed in detail in Chapter 2.

Aside from natural sources, in urban and suburban areas the most relevant contribution to the optical sky background is the light scattered from artificial light sources. The negative impact of light pollution is not limited to astronomical observations: the aftermaths of an excessively bright night sky affect human health as well as the environment, without considering economical and cultural effects. In western world light pollution has been constantly increasing for the last decades and is still growing today. Monitoring this form of pollution and its evolution is fundamental both from scientific and environmental point of view.

1.2   About this work

1.2.1   Scientific context

Sky background has been extensively discussed in the literature, both on the spectroscopic and photometric aspects. Typically works available in the literature focus on specific aspects or sources of the sky background. Among the few comprehensive works of the sky background as a whole I remark the review by *Leintert et al. (1998)* [17], which is one of the main sources of the first part of my work. Another valid work where natural sky sources are described in detail is *Noll et al. (2012)*[18].

Concerning natural sources, many of them have been extensively studied in the last century. Modern works typically consist on refining numerical values using more advanced instrumentation.

In the case of artificial sources, only in the last two decades astronomers started to systematically study such sources on a large scale, developing for this purpose new methodologies and instruments. To make some examples, several are the studies to monitor light pollution by taking photometric observation, see for example *Hänel et al. (2018)*[14]. One of the most famous devices for all-sky photometric observation is for example the Sky Quality Meter (SQM), widely used in Observatories around the world to constantly monitor the sky brightness conditions. As a reference see *Cinzano (2005)* [7].

In the literature are also available some studies on the sky spectrum of different astronomical sites, even though these works typically limit to identify the main spectral components observed in few frames taken appositely for this purpose, without further quantitative analysis. Among these works I remark *Slanger et al. (2003)*[23], *Sanchez et al. (2007)*[21] and *Zhang et al. (2016)*[26], that reported the sky background spectrum observed at the Lick, Calar Alto and Xinglong observatories respectively.

1.2.2   Aims of the work

The main purpose of this work is to characterize the sky background spectrum of the Asiago Astrophysical Observatory, Asiago, Italy. After the identification of the spectral features typical of each background source, the main goal is to study the evolution of the spectrum in the last years.

The actual distinctive point of this work is that I am using "recycled" data, i.e. I extract the sky spectra from frames originally taken to study astronomical objects. This strategy has the advantage that data is already available and no further observing time is required; moreover, the amount of data is *virtually* huge, since I may use every single spectral observation ever obtained in the site. Actually, on this work I used 35 spectra collected from 2006 and 2020 to test the concept.

The actual core of the work is the development of a data reduction pipeline, capable of automatically extracting from the original bidimensional spectra the information about the continuum and the emission lines available. The remarkable fact about the pipeline is that I tried to make it as automatic as possible, being able to correctly process frames taken in very different conditions. The idea behind this effort is to create a tool that can extract information automatically finds two main applications: 1) extend the dataset of this work using new frames without further effort and 2) create a tool that can provide a brief description on the sky condition during observations. The pipeline is implemented in Python 3.

1.2.3   Structure of the work

This work is divided into two main parts: in the first one are described the sources of the optical sky background: their emission mechanism, and the impact in the background in terms of distribution and intensity on the sky sphere. In particular after this introduction in Chapter 2 are described all the main natural sources and their effects. In Chapter 3 is discussed in general the light pollution, its negative impact and the effects on the astronomical observations. In the second part I present the original part of the work. In Chapter 4 I accurately describe the data extraction pipeline in all its parts. In Chapter 5 I actually analyze the extracted data to find different types of trends and correlations. Finally in Chapter 6 I take final conclusions on the work.

1.3   Units of measurement

In this section I explore the different units of measurement used in this work. Note that different research branches or different epochs may use different units. In this work I tried to be coherent and use the same units, eventually converting values provided in the original works with different units. For a more comprehensive description of the following units, refer to the works by *Leintert et al.* [17] and by *Cinzano* [3].

1.3.1   Photon counts

One of the most used unit to quantify light flux, in particular on higher energy frequencies, is using the photon flux the quantity

$$n = \int n_\lambda S(\lambda) \mathrm{d}\lambda \tag{1.1}$$

the sum over the wavelength of the number n_λ of photons crossing an unit area in a unit time, emitted in wavelength in the interval $[\lambda, \lambda + \mathrm{d}\lambda]$ from a solid angle unit and collected by a device of sensitivity S.

Another similar unit is the Rayleigh, defined as

$$1\,\mathrm{Rayleigh} = \left(\frac{1}{4\pi}\right) 10^6 \,\mathrm{ph/cm^2/s/sr} \tag{1.2}$$

1.3.2   Energy units (intensity)

Specific intensity is defined as the amount of electromagnetic energy $\mathrm{d}E_\lambda$ (emitted in the wavelength interval $[\lambda, \lambda + \mathrm{d}\lambda]$) flowing trough a surface $\mathrm{d}A$ in a direction between the solid angle $\mathrm{d}\Omega$ tilted by the angle θ with respect to the normal of the surface in the time $\mathrm{d}t$., i.e.

$$I_\lambda = \frac{\mathrm{d}E_\lambda}{(\cos\theta \mathrm{d}A)\mathrm{d}\lambda \mathrm{d}\Omega \mathrm{d}t} \tag{1.3}$$

Assuming all the photons are emitted roughly at the same wavelength, called effective wavelength λ_{eff} the energy carried by a photon flux is

$$dE = \frac{hc}{\lambda_{\text{eff}}} n_{\text{eff}} dA d\Omega dt \tag{1.4}$$

Assuming a typical $\lambda_{\text{eff}} = 5500\,\text{Å}$ for the V band in the visible spectrum then

$$I_{(V)}[\text{W}\,\text{m}^{-2}\,\text{sr}^{-1}] = 3.578 \times 10^{-15} n_{5550}[\text{ph}/\text{cm}^2/\text{s}/\text{sr}] \tag{1.5}$$

1.3.3 Photometric units

Unit definitions. Photometric units are based on the fundamental definition of candela in the international measurement system.

- 1 cd is the intensity (energy flux per solid angle) emitted by a black body at 2045 K from a surface of $1/600\,000\,\text{m}^2$ under a standard pressure of 1013.25 ha Pa.

- Luminous flux $d\Phi$ that emits under a solid angle unit $d\Omega$ are related to the luminosity I by the relation

$$I = \frac{d\Phi}{d\Omega} \tag{1.6}$$

  where flux can be expressed in lumen (lm) (then $1\,\text{cd} = 1\,\text{lm}/\text{sr}$).

- Luminosity is defined as the luminous flux per unit area

$$l = \frac{d\Phi}{dA} \tag{1.7}$$

  and is usually expressed in Lambert (L), where $1\,\text{L} = 1\,\text{lm}/\text{c}^2\text{m}$.

- The brightness is the flux emitted per unit of solid angle, per unit area

$$b = \frac{d\Phi}{d\Omega dA \cos\theta} \tag{1.8}$$

  where θ represents the angle between the normal of dA and the direction of the source. Brightness is expressed in $\text{lm}/\text{m}^2/\text{sr}$ or equivalently in $\text{cd}\,\text{m}^{-2}$.

Conversions. Knowing the shape of the emission of a source it is possible to compute the energy flux equivalent to a given luminous flux. For a black body $1\,\text{lm} = 1.470 \times 10^{-3}\,\text{W}$, which means

$$b[\text{cd}\,\text{m}^{-2}] = 6.803 \times 10^2 b[\text{W}\,\text{m}^{-2}\,\text{sr}^{-1}] \tag{1.9}$$

Another useful conversion is between brightness and photon flux. At the effective wavelength of 5550 Å we have

$$b[\text{cd}\,\text{m}^{-2}] = 2.43 \times 10^{-12} n_{5550}[\text{ph}/\text{cm}^2/\text{s}/\text{sr}] = 0.103 n_{5550}[\text{ph}/\text{cm}^2/\text{s}/\text{arcsec}^2] \tag{1.10}$$

while for the V band the two the correction is slightly different:

$$b[\text{cd}\,\text{m}^{-2}] = 2.925 \times 10^{-12} n_V[\text{ph}/\text{cm}^2/\text{s}/\text{sr}] = 0.124 n_V[\text{ph}/\text{cm}^2/\text{s}/\text{arcsec}^2] \tag{1.11}$$

1.3.4 Magnitudes

A traditional way to express luminosity in astronomy is using magnitudes. To express brightness it can be used both mag/deg^2 or $\text{mag}/\text{arcsec}^2$, where $b[\text{mag}/\text{deg}^2] = \text{mag}/\text{arcsec}^2 - 17.78$. Photometric magnitude (e.g. here in the V band) is related to photon counts and luminosity by the relations

$$V[\text{mag}/\text{arcsec}^2] = 41.438 - 2.5 \log b[\text{ph}/\text{cm}^2/\text{s}/\text{sr}] \tag{1.12}$$

and

$$V[\text{mag}/\text{arcsec}^2] = 12.603 - 2.5 \log b[\text{cd}\,\text{m}^{-2}] \tag{1.13}$$

1.3.5   S10 system

Often the brightness of the sky is expressed as equivalent number of $10\,\text{mag}$ stars per square degree. Geometrical arguments lead to the equation

$$b[\text{mag/arcsec}^2] = 27.78 - 2.5\log b[\text{S10}] \tag{1.14}$$

which is valid in the visual band, for typically solar-like stars.

According to the observing band and the reference star, this conversion value can significantly vary, see for example Tables 1,2 and 3 from *Leinert et al. (1998)*[17]. For example to pass from S10 to photometric units in the visual band one shall apply

$$b[\text{cd}\,\text{m}^{-2}] = 0.7 \times 10^{-6} b[\text{S10}_{\text{vis}}] \tag{1.15}$$

Chapter 2

The natural sky background

Even when artificial sources are neglected, there are still several natural background (bkg) sources. In this chapter each contribution will be described in detail. In the plot on Figure 2.1 are reported, in logarithmic scale, the main bkg sources for a wide range of wavelengths, from UV to radio emission. In the next lines I will consider only sources relevant for optical observations.
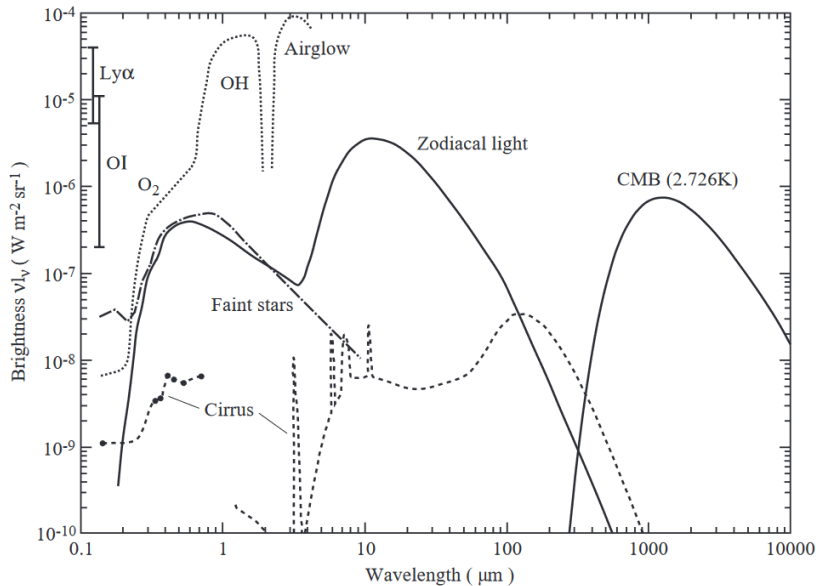
Figure 2.1: Different sky brightness contributions in different electromagnetic domains. In the optical band most relevant contribution are zodiacal light, airglow and faint stars. From *Leinert et al. (1998)*[17].

Photons produced by several bkg sources interact with dusts and aerosols in the Earth atmosphere leading to extinction and diffusion (scattering) phenomena. The total sky brightness can be quantitatively expressed as

$$I_{\text{sky}} = (I_A + I_{ZL} + I_{ISL} + I_{DGL} + I_{EBL})e^{-\tau} + I_{\text{sca}} \tag{2.1}$$

where A stands for airglow, ZL is zodiacal light, ISL integrated galactic light, DGL diffuse galactic light and EBL extragalactic bkg light. τ is the extinction coefficients and I_{sca} gathers all the scattering terms, i.e. light scattered from previous sources and from light pollution [17]. According to *Cinzano (1997)*[3] the total visual brightness of the natural sky ranges from about 220 to 120 $\mu\text{cd m}^{-2}$.

In this chapter I will analyze in detail all the terms in the equation (2.1).

2.1 Zodiacal light

Zodiacal light (ZL) consists of sunlight scattered by interplanetary dust particles. From the Earth it looks like a white glow visible during the twilight and extending from the Sun in the zodiacal region (see

Figure 2.2). Being reflected sunlight, the ZL spectrum is mostly identical to the solar one, at least in optic bands. It is the brightest bkg source in optical bands.

Figure 2.2: ZL after sunset at La Silla, Chile. Source: eso.org.

Figure 2.3: Isophotal map ot the ZL as $7100\,\text{Å}$. As a reference $1\,\text{S}_{10}/\square^\circ \approx 10^{-5}\,\text{cd}\,\text{m}^{-2}$ at those wavelengths (see [17, 3]). From *Frey et al. (1974)*[12].

Angular distribution. The figure 2.3, adapted from *Frey et al. (1974)*[12], describes the angular distribution of the ZL in ecliptic coo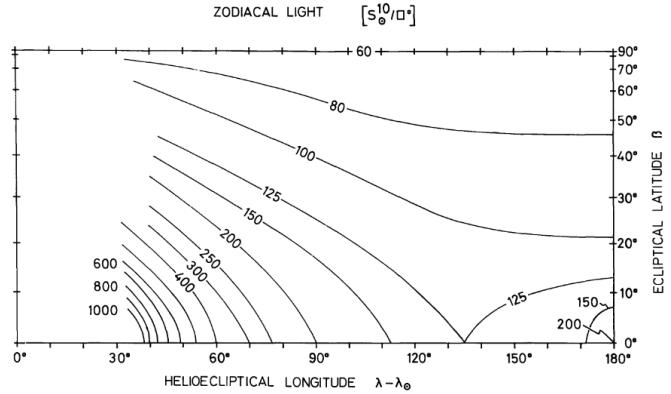rdinates. Such light is maximum along the ecliptic and close to the Sun. A fainter local maximum is present in direction opposite to the Sun. It is known as *gegenschein* and is produced by back-scattered solar light. ZL brightness varies from about $> 130\,\text{cd}\,\text{m}^{-2}$ on the ecliptic for angular distance from the sun $< 30°$ to a minimum toward the ecliptic poles of about $60\,\text{cd}\,\text{m}^{-2}$ [3]. Gegenschein maximum brightness reaches about $100\,\text{μcd}\,\text{m}^{-2}$. The contribution of ZL to the optical bkg is maximum during the twilight, after sunset in spring or before sunrise in autumn, from the northern hemisphere.

2.2   Airglow

The airglow is the faint emission on the higher layers of the atmosphere, produced by the interaction between atoms and the particles from the solar wind or by the chemical interaction between atoms. This is the second brightest natural optical bkg source after ZL.

Main mechanism. There are different channels that lead to airglow emission. Here I report some examples, [3].

- In the first layer between 85 and $100\,\text{km}$ most of the transitions involve the interaction of solar light with neutral species. We can find 2-body reactions such as

$$\text{H} + \text{O}_3 \longrightarrow \text{OH} + \text{O}_2 + \text{ph}$$
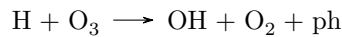
  Also 3-body reactions are possible. The typical example is

$$\text{O}{\equiv}\text{O}{\equiv}\text{X} \longrightarrow \text{O}_2 + \text{X} + \text{ph}$$
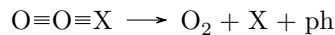
  where the species X that acts as a catalyst. These two reactions are responsible respectively for the OH and O_2 roto-vibrational bands in the near to medium infrared domain.

- In the upper part of the atmosphere, between 250 and $300\,\text{km}$, reaction between ionized species dominates. One of the brightest transition, the [OI] lines at 6300 and $6364\,\text{Å}$ are produced in the reaction

$$\text{O}_2^+ + \text{e} \longrightarrow \text{O} + \text{O} + \text{ph}$$
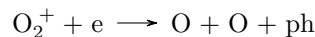
  An analogous reaction is responsible for other bright optical lines, such as the Na doublet at 5890,5896 Å.

- The outermost layers of the atmosphere, above $1000\,\mathrm{km}$, contain the most volatile elements such as ionized hydrogen that can produce typical HII transitions such as the Lyman and Balmer series.

A more comprehensive list of emission lines is reported in Table 2.1, [17].

Source	Wavelenght	Height
Lyβ	1026	geocorona
Lyα	1216	geocorona
OI	1304	250 - 300
OI	1356	250 - 300
O$_2$	3000-4000	90
[OI]	*5577*	*90*
Na D	*5890,5896*	*92*
[OI]	*6300*	*250 - 300*
[OI]	*6364*	*250 - 300*
Hα	*6563*	*geocorona*
pseoudocontinuum	*400 - 700*	*90*
O$_2$	8645	80
OH	6000-45000	85

Figure 2.4: Oxygen (green) and sodium (orange) airglow emission, photographed from the ISS. Source: eol.jcs.nasa.gov.

Table 2.1: Main airglow sources, emitting wavelengths and layer height. Italic rows are lines visible in the optic range, bold ones are the brightest. Adapted from Table 13 of *Leinert et al. (1998)*[17].

Angular distribution. Being produced by thin layers homogeneous on a large scale, the airglow emission is relatively uniformly distributed in the sky sphere, with an increase of brightness at high zenital distances due to the increase of geometric depth along the line of sight. In absence of atmospheric extinction the zenith brightness profile of a thin homogeneous layer at height h is provided by

$$I(z)/I(0) = \frac{1}{\sqrt{1 - [R/(R+h)]^2 \sin^2 z}} \tag{2.2}$$

where z is the zenith angle and R is the earth radius. Actually going toward the horizon atmospheric extinction is no longer negligible and above $z \approx 80°$ emission decreases again toward the horizon.

Variations in airglow emission. Airglow emission varies in time, both on short and long timescales, following the behavior of the atmosphere and the solar activity [17]. Emission is also related to the geomagnetic latitude: it is maximal in the subpolar region, at a latitude of about $60° - 80°$ after which it significantly drops. In the polar region airglow is substituted with auroral emission. In the low latitude regions emissions are generally low with a slight increase toward the equator, [9].

Spectral distribution. Airglow emission consists of a series of very bright spectral lines against some faint broad bands (pseudo continuum). Such spectral energy distribution makes the measurement of the total brightness in the optical bands not very significant as most of the light is produced in a restricted wavelength domain. The minimum value of integrated airglow brightness in visual bands is of the order of $35\,\mathrm{\mu cd\,m^{-2}}$, [3]. Nevertheless, the sky brightness at the specific emission wavelength is much higher than the reference value above and in sufficiently narrow bands can overwhelm the other sources.

2.3   Galactic background

In optical bands the third significant contribution to the bkg level is provided by unresolved stars in the Galaxy. The contribution of such sources depends on the ability to resolve the brightest stars [17], i.e. on the limiting magnitude of the instrument.

Angular distribution.   Unresolved stars follows the morphological structure of the Milky Way. The signal is higher toward the galactic plane and the galactic center. Its spectrum follows typical optical stellar spectra with the characteristic black-body emission. Typical optical brightness values range from about $200\,\mathrm{\mu cd\,m^{-2}}$ toward the region surrounding the galactic center $20\,\mathrm{\mu cd\,m^{-2}}$ toward galactic poles.

2.4   Further minor sources

The three components above (ZL, airglow and unresolved stars) are the main components that dominate the sky natural bkg in the optical domain. There are still some sources much smaller than the main ones but yet detectable.

2.4.1   Diffuse galactic light

Similar to the ZL, it is the result of the scattering of stellar emission with interstellar dust particles. *Leinert et al.* estimate its contribution as between 15% and 30% of the total integrated light from the galaxy, according also to the observing wavelength, [17]. This estimation is rather uncertain because of the faintness of the radiation and the contamination of direct stellar light. There are no comprehensive maps for the diffuse galactic light but it is very likely this emission to be concentrated along the galactic disk, analogously to the direct stellar component. Its spectral energy distribution is comparable with stellar spectra, since its nature of stellar reflected light. We can state expected diffuse light produces a brightness of the order of 15 to $5\,\mathrm{\mu cd\,m^{-2}}$, [3].

2.4.2   Extragalactic background

A much smaller contribution is led by the extragalactic bkg, i.e. emission of faint and or unresolved galaxies. It is very difficult to quantify the resulting brightness and in many cases only the upper limits for extragalactic bkg are available. The main estimation difficulties are due to the faintness of the signal and with respect to the other sources. The order of magnitude the visual brightness upper limit is at least $0.7\,\mathrm{\mu cd\,m^{-2}}$, [3].

2.5   Atmospheric extinction and scattering

Particles in the Earth atmosphere can interact with the incoming radiation causing extinction and scattering (or diffusion) phenomena. Let us consider a light beam with intensity I_0 that travels through a medium for a distance l. We define the extinction coefficient κ as the amount of radiation absorbed by the medium per unit length. If we assume that absorption occur only due to reflection phenomena (and no radiation energy is held by the particle), then the solution of the radiative transport equation states that the intensity of the beam after a distance (or geometric depth) l in the medium is simply

$$I_{\mathrm{ext}} = I_0 e^{-\tau} \tag{2.3}$$

where $\tau = \kappa l$ is called optical depth of the medium. The phenomenon of dimming of the light beam through a medium is called extinction. The radiation absorbed by the particles is totally re-emitted in a random direction, generating a diffuse component in the directions off the beam, which is the scattering. Numerically the total scattered light is

$$I_{\mathrm{sca}} = I_0(1 - e^{-\tau}) \tag{2.4}$$

i.e. the complementary of the extincted component. Even if extinction and scattering are the two sides of the same phenomenon, for my purposes the attention is focused mainly on scattering, which is capable of producing a diffuse radiation component where no direct sources are present.

2.5.1   Scattering mechanisms

According to the size of a medium particle with respect to the radiation wavelength, two different scattering mechanisms can occur. Small particles like molecules produce the Mie scattering while larger solid particles are responsible for the Rayleigh scattering.

Rayleigh scattering. This is due to the interaction of light with particles smaller that the wavelength: if the particle is small enough the phase difference of the beam along the particle is negligible and the it "sees" in each moment an homogeneous electromagnetic field. The particle will be forced by the beam to emit as an oscillating dipole, in phase with the beam and with the same wavelength, but in a random direction. From the dipole theory, when a light beam of intensity I_0 travels through a medium, meeting N particles of polarizability α, the scattered intensity of the beam is

$$I_{\mathrm{Ray}} = I_0 \frac{8\pi^4 N\alpha}{R^2} \frac{1 + \cos^2\varphi}{\lambda^4} \tag{2.5}$$

where λ is the wavelength of the radiation and φ the angle between the beam and the observing direction. Note that it steadily decreases at increasing wavelengths ($\propto \lambda^{-4}$), i.e. Rayleigh scattering is stronger in the blue than in the red bands. Concerning the angular distribution of scattered light, the intensity is maximum both along the original beam direction (*forward scattering*) as well as in the opposite direction, back to the source (*back scattering*). Minima are located at 90° from the maxima.

In the optical regime, Rayleigh scattering is produced by the air molecules themselves. This form of scattering is responsible for the blue sky in daytime and for twilight. It is also the main cause for atmospheric extinction, in particular at shorter wavelengths.

Mie scattering. Mie scattering occurs when light meets particles of size comparable or larger than the characteristic wavelength. In this case different parts of the particle experience different intensities of the electromagnetic field; each portion of the particle will emit as a single dipole, locally in phase with the beam, and the total emission will be the result of the interference pattern between all the portions of the particle. In this case only the wavelength of the original beam is preserved, while phase is distorted and direction is random. The numerical expression of Mie scattering is rather complex and involves the solution of Maxwell equation; several numerical or empirical relations are available in the literature. For our purposes it is relevant to say that the intensity of Mie scattering is proportional to $\propto \lambda^{-0.8}$. Moreover, most of the light is scattered along or close to the beam direction, i.e. the forward component is dominant (the larger the particle, the more relevant the forward component).

In the atmosphere Mie scattering is produced by solid particles suspended in the air (*aerosols*), such as dust grains, smoke or water drops. In the figure 2.5, from *Tüg (1977)*, are reported the extinction coefficients for Rayleigh and Mie scattering (the latter labeled as "aerosols") [24]. It is clear that Mie scattering is negligible with respect to Rayleigh one, in particular at shorter wavelengths. This is true only in clear sky conditions, with an atmosphere locally without fog, smoke or other pollutants, that may significantly raise the impact of Mie scattering.

2.5.2 Effects on the sky brightness

Every light source is responsible for a certain amount of light scattering. Depending on the site and the observation time, the effects of scattering on the total sky brightness can vary significantly. The three most significant effects of scattering on the optical bkgs are

Diffusion of natural sources In a dark site most of the scattered light is produced by airglow, ZL and the galactic bkg which are the brightest "direct" light sources.

Diffusion of artificial sources Atmospheric light scattering is the main mechanism responsible for light pollution when far from the light source. Due to Earth curvature, geographic features and atmospheric extinction the direct light contributes to pollution only when very close to the light source. As reported in Chapter 3, brightness of scattered artificial light from a city varies with the population and the distance.

Diffusion of Sun and moon light As said before Rayleigh scattering is responsible for the twilight: even if the Sun is below the horizon some residual scattered light still brightens the sky. Conventionally astronomical twilight ends when the sun is 18° below the horizon and other light sources, such as ZL, become more relevant.

A similar effect is provided by scattered moonlight. Such light brightness depends on the lunar phase and on the distance between the Moon and the observing position in the sky. According to [16] and similar sources, in optical bands scattered moonlight can lead to an increase of the sky brightness of one order of magnitude. A typical dark site have a visual brightness of the order of $1.5 \times 10^{-4}\,\mathrm{cd\,m^{-2}}$ (corresponding to $V = 22\,\mathrm{mar/arcsec^2}$) the presence of the full moon can raise the value up to $2.5 \times 10^{-3}\,\mathrm{cd\,m^{-2}}$ (i.e. $V = 19\,\mathrm{mar/arcsec^2}$).
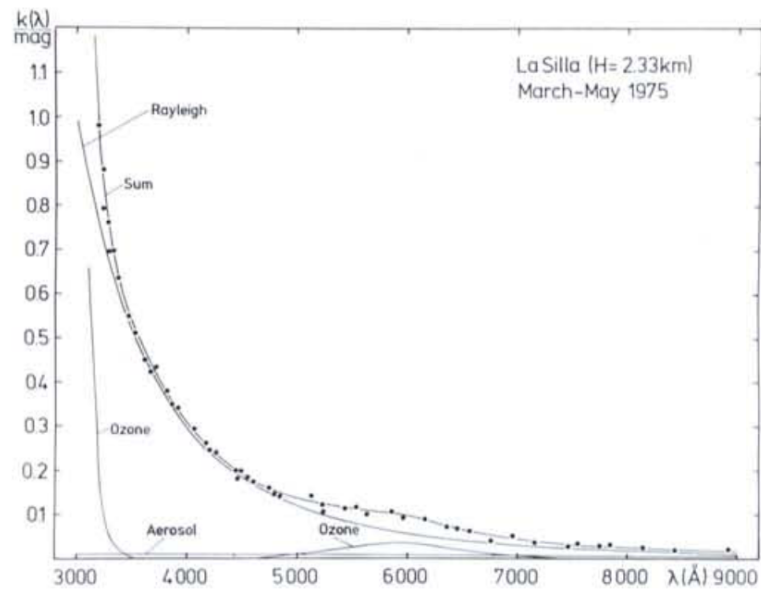
Figure 2.5: Extinction coefficients for Rayleigh and aerosol (Mie) scattering. The former component dominates over the latter at all the wavelengths, in particular for shorter ones. From *Tüg (1977)*[24].

Chapter 3

Artificial sky light pollution

In this chapter I will present the light pollution (LP) in detail and its effects on the night sky. Most of the following content is based on *Cinzano (1997)*[3] with integration from more recent works.

3.1 Introduction to LP

Definitions. Light pollution is the dispersion on the sky of artificial light sources (see Figure 3.1). A different concept is the optical pollution, i.e. the one produced by an artificial source that directly illuminates an area or a person not required to. Optical pollution is thus a component of the LP; the other fundamental one is the indirect light scattered by the atmosphere. Direct light concurs to LP when close to the source, the diffuse component can propagate LP very far from the original source.

Figure 3.1: Heavily polluted sky observed in the commercial area of Mestre, Venice. Only Sirius (top left) and few other stars are visible. Note the high brightness contrast between the tree in the foreground and the sky. Source: own work.

Note that also unnecessary artificial lights are considered LP. Every form of artificial illumination, if not motivated by safety or necessity reasons should be limited as much as possible [3].

Brief history of the LP. For millennia mankind observed the night sky, limited only by the atmospheric conditions. First reports of the effects of artificial lights started in the 19th century, during the urban expansion of European cities to the industrial revolution. With the spreading of electrical illumination at the beginning of the 1900, faintest stars and the zodiacal light became invisible in largest urban centers. Initially astronomers bypassed the problem by moving observatories from the city to rural dark areas.

Starting from the 60s, the steady increase of population in western countries led to a further significant increase of the LP so that dark sites were always fewer and many of the old observatories were already strongly limited by LP. Only at that time astronomers started being concerned about the problem and

that finally focused the attention on how to control and eventually limit the amount of light dispersed in the sky.

In the 70s the work of some major US astronomical observatories in raising the awareness of citizenship on the LP problem led to the creation of the first laws and regulations against LP. In 1973 the International Astronomical Union (IAU) created a commission aimed to identify and protect dark astronomical sites and in 1976 approved a resolution that asked authorities to take measures to protect and preserve astronomical observatories. The requests of astronomers were only partially accepted and in 1988 another IAU resolution was approved, asking again for urgent measures to contrast LP.

During the 80s the awareness of LP was mature. Experimentation on more efficient light systems started and some pioneering laws were approved. Astronomers created associations and projects to monitor the LP, such as the International Dark-Sky Association (born in 1988). Informative campaigns continued in the 90s, when interest started developing also for the ecological and medical impact of LP. From that decade LP outcomes started to be studied by other scientists, such as biologists or doctors. Laws against LP spread both on local and national levels in many western countries, although in many cases they proved to be inadequate to limit the problem.

In the last decade the LP concern arose with the introduction of LED lights that proved to be potentially harmful to human health (see below). At the same time the development of new technologies and instruments, such as low-cost light sensors and all-sky cameras, allowed a more capillary monitoring of the phenomenon, both on spatial and temporal scale.

According to current observations, despite all the efforts, the amount of artificial light dispersed in the night sky is still increasing.

3.2 LP sources

In this section I report which are the main responsible for LP and which kind of sources they are.

3.2.1 Impacting illumination systems

The different types of night light systems concur differently to the total LP amount. Due to safety or necessity requirements, some lighting systems naturally disperse more light toward the sky than others. Nevertheless in many cases some measures can be taken to limit the impact of these systems.

Roads. To be able to distinct objects on a dark background there must be a sufficient light contrast. The strategy used in road illumination consists of brightening the road where the object is distinguishable as a dark shadow. The issue of this strategy is that a large fraction of the light, after hitting the road surface, is dispersed upwards. Moreover, if the light sources are not shielded or the system is not designed properly, a fraction of the produced light is directly lost towards the sky. To reduce the impact of LP lamps should illuminate as much as possible the road, avoiding unnecessary dispersion in nearby areas. Choosing properly shielded lamps increases the efficiency of the system and significantly reduces the amount of light directly dispersed upwards.

Sport facilities. Illuminating sport facilities is fundamental to increase their use time; moreover, physical activities are doubtless fundamental for the physical and mental health of individuals. Adequate illumination is necessary for the optimal perception performance by the human eye, fundamental in sport activities. Adequate illumination is required also for the public to be able to follow the event. For their peculiar necessities the room for improvement in the LP reduction in these facilities is limited. For example the illumination systems should be able to adequate themselves to the type of activity: the necessities for a high level competition are very different with respect to those of ordinary training activity.

Buildings and monuments. The main reasons to illuminate a building or a monument are to give value to historical or artistic heritage, highlight architectural features or for safety and commercial purposes. The light design must be carefully studied to fit and give value to the building or monument. To reduce LP impact of these sites few basic precautions can be taken, such as 1) avoid light beams that exceeds the limits of the illuminated structure, 2) design illumination to send the maximum amount of reflected light towards the point from which the site is observed and avoid excessive dispersion in other directions and 3) excessive levels of illumination should be avoided.

3.2.2   Types of light sources

The impact of a light source depends on multiple factors, such as its spatial and the spectral energy distribution.

Spatial emission and mitigation strategies

Goniophotometers.   It is possible to measure the light spatial distribution produced by a source using the so-called goniophotometer, i.e. a device capable of measuring the intensity of the light emitted by an object at different angles. Let C be the angle between the planes containing the observing and a reference direction (typically the road axis direction); γ is instead the angle between the vertical to the light source and the observing direction. For a visual reference see Figure 3.2.
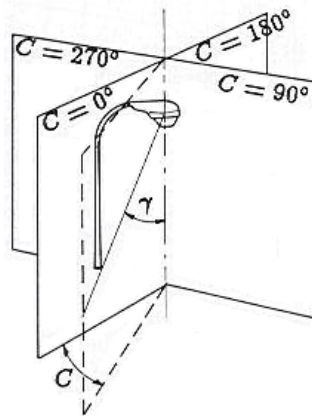

Figure 3.2: Scheme of the angles used in the representation of goniophotometer measurements. The plane defined by $C = 0$ is parallel to a reference direction, typically identified by the road axis, [3].

Reduction of dispersed light.   There are many strategies to improve the efficiency of light systems and reduce the amount of vertically dispersed light.

- *Avoid direct vertical illumination* (i.e. no light emitted for $\gamma \geq 90°$), using reflector devices such as aluminum mirrors. Devices like the old globe lamp posts present probably the worst illumination properties: most of the light is directly sent upwards, while the vertical metal support casts a shadow on the surface around the post. This is not only very impacting on the LP, but also an important waste of energy (see Figure 3.3 for a comparison between the two versions). A similar argument can be done with old lanterns, where most of the light is directed sideways and upwards.

  Even if effort was made to reduce the impact of the public urban furniture, by shielding these old devices significantly cutting the upward direct emission, it is not rare to still find them devices in private properties.

- *Direct light only toward the area to be illuminated*, to avoid unnecessary upward light dispersion from the illuminated area. Optimal illumination can be obtained both by orienting the light source toward the wanted area and by properly modeling the intensity of the light beam, using asymmetric projectors. In Figure 3.4 are reported two examples. In both cases a good alignment is necessary to avoid the direct upward dispersion.

- *Use appropriate illumination levels.* Each activity that requires artificial lighting comes with its own optimal illumination. Exceeding that level does not lead to any improvement or can even have negative effects. Excessive illumination can lead to sight discomfort, dazzle and loss of contrast in the illuminated object, as well as increase the amount of dispersed light.

Spectral energy distribution

According to the type of source the dispersed light can have a different impact on the LP. It follows a list of the different types of lamps available.
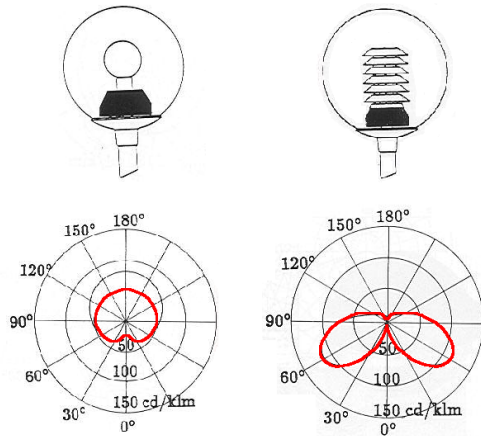
Figure 3.3: Effect of the shielding on a globe lamp. In the unshielded version (left) most of the light is directly dispersed upwards, without any benefit for the illumination. The shield (right) allow to reflect downwards most of the light, increasing the performance and decreasing dispersed light. Adapted from *Cinzano (1997)*[3].
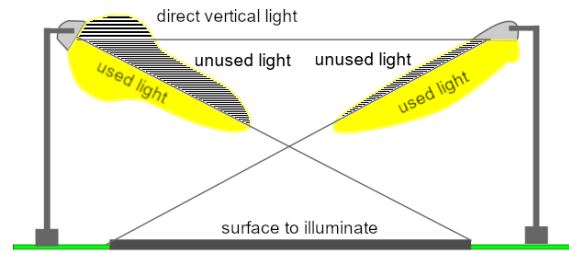

Figure 3.4: Example of light posts for road illumination: a generic lamp with a symmetric beam (left) tends do disperse or not employ a significant fraction of the total light produced; designing a lamp with the proper orientation and beam shape (left) increases the efficiency by illuminated only the desired area. Adapted from *Cinzano (1997)*[3].

Incandescent lamps They are based on the heatening of a tungsten filament due to the passage of electric current. The filament reaches temperatures of the order of 2700 K and emits nearly as a black body in the visible and IR spectrum, producing a yellow-withe warm light. Due to the continuum emission in the visible spectrum, they were particularly impacting on the sky pollution. They got progressively dismissed due to their low efficiency (≈ 10 lm/W) and limited lifetime.

Mercury vapor lamps In these lamps mercury vapors are excited by an electric arc and emit in the UV domain. The lamp is surrounded by a fluorescent material that redistributes the radiation in the visible range. Due to the continuum emission in the visible range, these lamps are very pollutant and are banned by all the LP laws. Due to their low efficiency, of about 50 lm/W, in the 90s most of them were dismissed too.

Metal-halide lamps These are the evolution of mercury lamps but with the addition of metal halides that improve the efficiency (up to 100 lm/W) and color rendition. They are highly pollutant in all the bands of the visible spectrum and their use is strictly regulated by anti-LP laws, where present.

Low-pressure sodium lamps Also known as LPS. In these lamps light is produced exclusively by the emission of the sodium doublet 5683-5688 Å, after stimulation by an electric discharge. Their efficiency is very high (up to 200 lm/W) but their emission is monochromatic and do not allow to see colors. These lamps are among the least pollutant as the emission occurs in a very limited portion of the spectrum, see Figure 3.5; for example photometric bands U and V are not even touched by LPS emission. Their diffusion was not homogeneous and in some countries, such as Italy, they never widely spread, in favor of HPS lamps (see below). They are progressively disappearing, replaced by new technologies.

High-pressure sodium lamps Known also as HPS. Similar to the LPS variant, work at a higher pressure to obtain a continuum emission that allows color perception, at the cost of a lower efficiency and more pollutant effect. Nevertheless, in typical HPS lamps spectrum is produced most of its effect in the region between 5400 and 6500 Å and is totally irrelevant below 4500 Å and in the photometric B band, see Figure 3.5 for a visual reference. These lamps are still widely used in Italy, even though in the last decade have started being replaced with LED (see below), that have better efficiency and color color rendition.

LED lamps These are the latest technology whose massive application began in the last decade. LED, acronym for Light-Emitting Diode, consist of a doped semiconductor capable of emitting light at
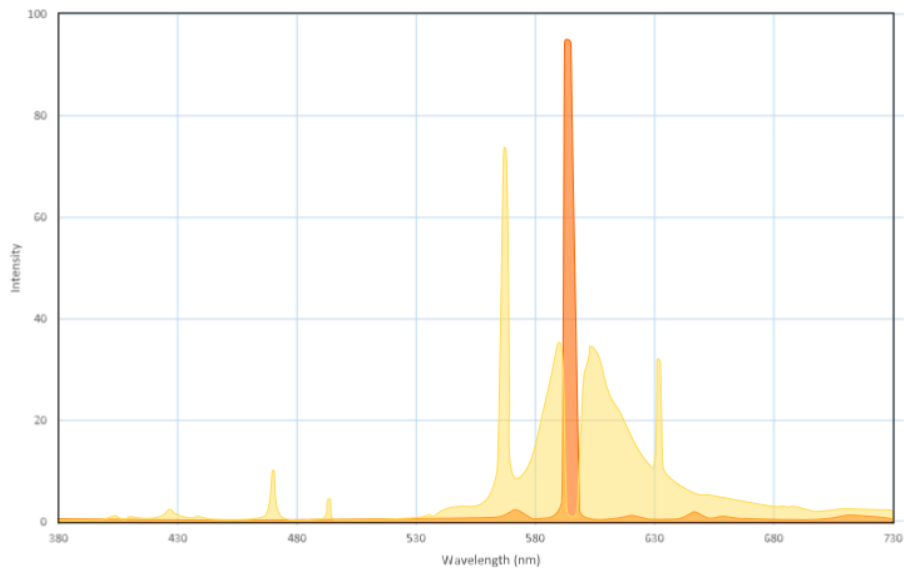
Figure 3.5: The spectrum of sodium-vapor lamps: in yellow HPS and in organge LPS are shown. Source: own work.
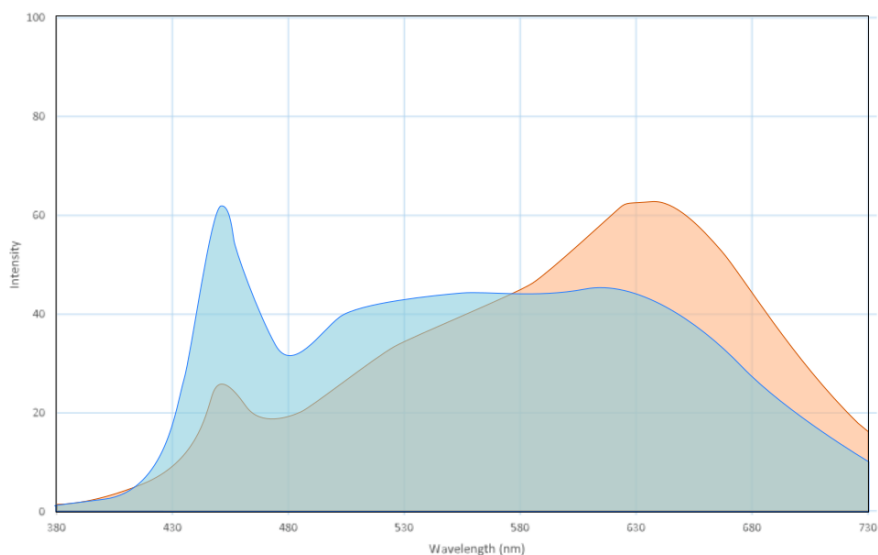

Figure 3.6: The spectra of a warm-white (the red plot) and cold-white (blue plot) LED lamp. According to the type of fluorescent coating the amount blue light re-emitted at red wavelengths can vary, producing warmer or colder tonalities. Source: own work.

the passage of an electric current. In typical white LEDs emission occurs in the blue domain and part of it is absorbed by a fluorescent coating and re-emitted in the yellow; the eye perceives such mixture of blue and yellow as a white color. Changing the composition of the fluorescent different white tonalities can be produced. Most efficient LED devices have efficiencies comparable with LPS lamps (200 lm/W) and their white emission allows color perception, unlike LPS. Due to the high range of wavelength emission their polluting effect is significant. Moreover, the blue emission they present at about 4500 Å contaminates a part of the spectrum not touched by sodium-vapor lamps, impacting on the photometric U band, the last visible one not contaminated by sodium lamps. Blue emission has also a significant impact on human health, as described below (see section 3.4).

3.3   LP propagation models

After the analysis of the source of LP in this source I will discuss how photons dispersed toward the sky propagate into the atmosphere. As said earlier, LP is constituted by two components: direct light from a source (both a lamp or an illuminated surface) and the indirect light scattered by the atmosphere. Currently, different works modeled the behavior of LP as a function of other measurable parameters. In this section I will expose the most relevant results from the literature.

3.3.1   The Walker's law

In one of the seminal works on the topic, *Walker (1977)* derived an approximate empirical relation between the intensity of sky brightness I, population of a city P and the distance d from that city [25]. The Walker's law is the following

$$I = c \cdot P \cdot d^{-2.5} \tag{3.1}$$

where the value of the calibration constant c depends on the units and photometric bands considered. The law was derived starting from 8 cities in California in the 70s and is still to predict the order of magnitude of LP in a given site.

3.3.2   The Garstang model

The first theoretical model of LP propagation is *Garstang (1986)*[13] and is based on geometrical and physical arguments.

The model. Referring to the original scheme, reported in Figure 3.7, a city is modeled as a circular disk of center C and radius R with homogeneous emission, directly proportional to the number of habitats. Direct upwards emission is a constant fraction of the total emission. An observer O at height A with respect to the city-disk observes the sky in a generic direction identified by OQ, characterized by the zenith distance z and azimuth from C equal to β. A photon emitted by a point X on the city can concur to the sky brightness along OQ only if scattered (for the last time) in a point Q and distance u to O. When traveling from X to Q part of the light is diffused due to extinction, and the same occurs between Q and O. Moreover, when in Q, only a fraction of light is scattered exactly toward O. Note extinction and scattering are modeled as a function of the amount of molecules and aerosols in the atmosphere, which depends on the height at which these phenomena occur. A correction is also performed to account for double scattering interactions.

The total amount of light collected in the direction OQ is the sum of all the contributions from the disk surface at different distances u on the line of sight.

Total luminosity from a city. The functional form the generic sky brightness is very long and elaborate and I decided not to report it in this work. More interestingly, the model provides an indication of the total upward intensity from a city in the direction θ from the horizon with respect to the vertical:

$$I(\theta) = I_0 \left[2G(1-F)\sin\theta + 0.554F \left(\frac{\pi}{2} - \theta \right)^4 \right] \tag{3.2}$$

where F is the fraction of light directly dispersed upwards, while G is the fraction dispersed after ground scattering. The first term of the equation contains the contribution from the indirect component, the second is the direct one.
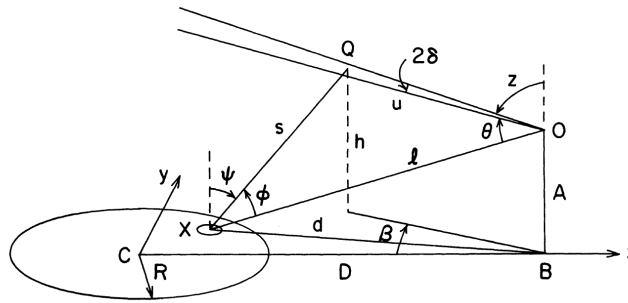
Figure 3.7: Scheme of the model by Garstang, where all geometrical quantities are highlighted. From *Garstang (1986)*[13].

Dependence on the atmospheric conditions. In the Garstang model the atmospheric condition can be modeled as a function of a scale parameter K, defined as the ratio between aerosols and molecules at the city ground level. As shown in Figure 3.8, the model correctly predict that in case of hazy conditions ($K = 2$ in the example of the figure) brightness close to the city is increased and decreased going further, with the respect to clear conditions (e.g. $K = 0.5$). The former effect is due to enhanced scattering, the latter due to enhanced extinction on longer optical depths.
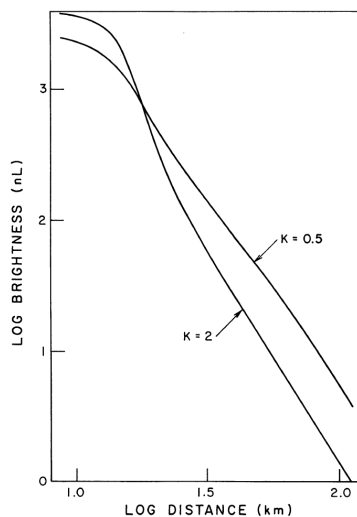
Figure 3.8: Sky brightness as a function of the distance, for clear ($K = 0.5$) and hazy ($K = 2.0$) skies. A larger amount of aerosols "shields" the light above the city, making a darker sky at higher distances. From *Garstang (1986)*[13].

3.3.3 Cinzano model

Due to the lack of systematic studies on the intensity emission as a function of the zenith angle, the Garstang model is still debated and with time some variants have been proposed.

In *Cinzano (1998)* it is argued that the reflected component would have to be isotropic due to diffusion on both horizontal and vertical surfaces such as streets and walls [4]. The proposed correction to the original model is

$$I(\psi) = I_0 \left[2G(1 - F) + 0.554F \left(\frac{\pi}{2} - \theta \right)^4 \right] \tag{3.3}$$

Note in this case if we fix F and G then the Cinzano function returns higher intensity values, as shown in Figure 3.9, because more importance is given to the direct or directly diffused component even at small angles. Such contribution, according to the author, is originated by multiple Lambertian reflections both on the horizontal (streets, squares) and vertical surfaces (walls and buildings). Each single reflection

is Lambertian and occurs on a surface with a random inclination, when light from all the reflections is integrated the result is an isotropic distribution.

Figure 3.9: Comparison between Garstang and Cinzano functions (respectively blue and red solid lines). The main difference is the modeling of the direct component, Labertian for the former, isotropic for the latter. Source: own work.

Qualitative observations seem to confirm that the direct contribution is actually as relevant as predicted (once we excluded the lowest observation angles, where shielding effects from the buildings are not negligible).

3.4   Negative impacts of LP

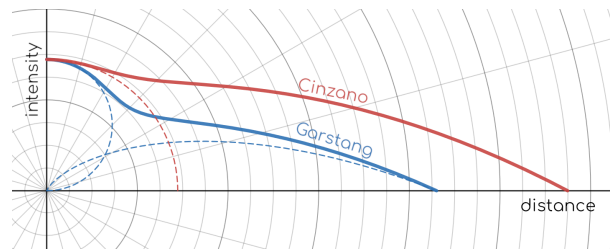**Effects on human health.**   Light exposure in night time interferes with the circadian rhythm, i.e. the natural metabolic processes that regulate the sleep-wake patterns. Light exposure during night time significantly reduces the natural production of melatonin, an important hormone that regulates many biological mechanisms. Among the most important functions, melatonin regulates sleep and helps the prevention of some forms of cancer. Melatonin deficiency has been proved in fact to be strictly correlated with higher incidence of breast and prostate cancers as well as be the main cause of many sleep disorders.

Melatonin decrease is proportional both to light intensity and frequency. A greater effect is given by brighter and bluer sources. In this context the spreading of LED lights, with their strong emissions in the blue side of the visible spectrum, is considered a concern by many health associations and experts.

Effects on the environment.   LP affects other living beings as well as humans. Animals exposed to abnormal levels of light at night change their behavior and habits. Note this form of pollution is probably the most widespread but yet one of the least acknowledged.

Economical effects.   A lighting system that disperse radiation toward the sky is not very efficient from the energetic point of view, since part of the energy is wasted in photons that are not actually lighting anything if not the sky. To compensate for the upward loss of radiation it is necessary to increase the size or the power of the light source, requiring a higher energy consumption.

In 1994 about 1 TW h of electrical energy has been wasted in light dispersed directly or after bouncing on the enlightened object citecinzano1997inquinamento. Current data tells us that in Italy, 6 TW h of energy were employed for public illumination in the 2017, corresponding to 1.7 bln €, [8, 11]. I can assume that 15% of emitted light is directly dispersed toward the sky and another 15% is dispersed after the reflection with the enlightened object, [3, 13]. A further assumption is that public illumination accounts for 50% of the total night artificial lighting [19]. Under these assumptions I can conclude that only in 2017 1 bln € in electric energy was wasted.

Unluckily, in the last years efficient light sources like LEDs allowed the production of powerful illumination systems at low cost making the economical argument less relevant. If light is cheaper, it is less critical whether part of it is lost toward the sky.

Cultural effects.   All the cultures around the world developed myths and legends involving the heavens; night sky inspired artists and philosophers in western cultures for centuries and in general the observation of a starry sky always belonged to the human experiences. With the increasing urbanization and LP a larger fraction of the world population no longer have access to a clear night sky (see next section, 3.5). In terms of traditions and human experience this is a great loss, but yet difficult, or impossible, to quantify.

Scientific effects. The increase of the night sky brightness has negative effects on astronomical observations. In particular a bright background decreases the quality of the collected data by decreasing the signal-to-noise ratio (SNR), i.e. the ratio between the astronomical signal S and the total noise N.

Let us consider a faint astronomical source with a photon flux (per unit area, unit time and wavelength) equal to s_*. The astronomical signal over the integration time t is simply $S = s_* \cdot t$. For a weak source and a long exposure time the most significant noise source is the photon shot noise, i.e. the square root of the total signal. Let s_{sky} be the sky photon flux; if the source is faint $n_* \ll n_{\text{sky}}$. The SNR is

$$\text{SNR} = S/N = \frac{s_* \cdot t}{\sqrt{(s_* + s_{\text{sky}})t}} \approx \frac{s_*}{\sqrt{s_{\text{sky}}}}\sqrt{t} \tag{3.4}$$

which means that $\text{SNR} \propto \sqrt{t}$; increasing the exposure time the SNR improves too. Actually it is not possible to increase t arbitrarily: each pixel in the detector can record a finite number of photons before saturating. If S_{max} is the maximum signal that can be collected before saturation, then the maximum exposure time achievable is

$$t_{\text{max}} = \frac{S_{\text{max}}}{s_* + s_{\text{sky}}} \approx \frac{S_{\text{max}}}{s_{\text{sky}}} \tag{3.5}$$

and this correspond to a maximum SNR of

$$(S/N)_{\text{max}} = \frac{s_*}{\sqrt{s_{\text{sky}}}}\sqrt{t_{\text{sky}}} = \frac{s_*}{\sqrt{s_{\text{sky}}}}\sqrt{\frac{S_{\text{max}}}{s_{\text{sky}}}} = \sqrt{S_{\text{max}}}\frac{s_*}{s_{\text{sky}}} \tag{3.6}$$

i.e. the best SNR is inversely proportional to the flux of the sky. On a polluted site it is harder to obtain high SNR and it is more difficult to identify and observe faint objects. To sum up, we can state that a bright sky decreases the limit observing magnitude.

3.5 Distribution and evolution of the LP

3.5.1 Worldwide distribution

The *New World atlas of artificial night sky brightness*, by *Falchi et al. (2016)* [10], is a recent powerful tool that allows us to investigate the entity of LP around the world. LP heavily affects northern America, Europe and eastern Asia, see Figure 3.10. Most polluted areas in the world are the metropolitan area in the US east coast in America, the Benelux and northern Italy in Europe, the Nile region in Africa and South Korea and the Chinese coast in Asia. In these large areas most of the night sky features are completely lost and only a few brighter stars can be observed.
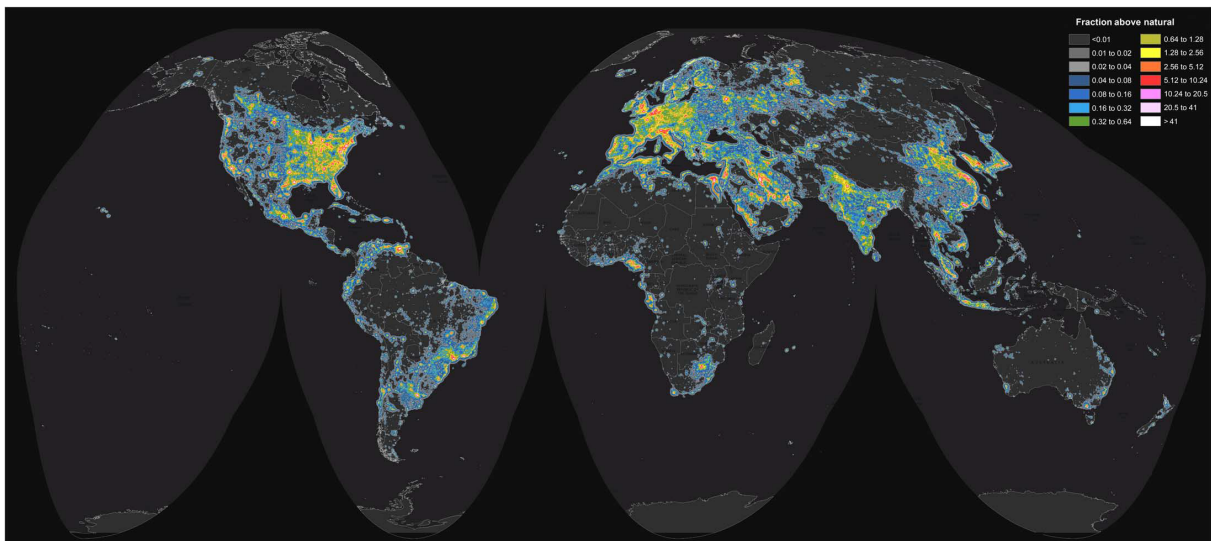

Figure 3.10: Night sky pollution distribution in the Earth, expressed as brightness fraction above natural sky level. From *Falchi et al. (2016)*[10].

In Table 3.1 I reported the percentage of populations living under skies with different brightness levels. I compared the global situation with the one in the European Union and in Italy. It is clear that the

situation of Europe is dramatic, with about two thirds of the population that live under a sky where faintest stars and the Milky Way disappeared; the situation in Italy is possibly worse.

Sky brightness (μcd m^{-2})	Effect	% population		
		World	EU	Italy
≤ 1.7	no contamination	8.0	0.0	0.0
> 14	impact on observations	83.2	100.0	100.0
> 87	Milky Way is not visible	63.7	94.0	99.6
> 688	few stars are visible only	35.9	59.5	76.9
> 3000	extreme pollution	13.9	20.5	26.7

Table 3.1: Fractions of the citizens in the world, European Union and Italy living under a sky with a given brightness. Adapted from *Falchi et al. (2016)*[10].

3.5.2 In Italy

Current situation. According to the data of the Word Atlas, Italy is the country with the most polluted skies, together with South Korea [10]. The Table 3.2 is analogous to Table 3.1 but focused on the fraction territory under a given sky pollution condition, instead of the population. According to the data, no portion of the Italian territory presents low or absent contamination.

Sky brightness (μcd m^{-2})	Effect	% area
≤ 1.7	no contamination	0.0
> 1.7	visible but small contamination	100.0
> 14	impact on astronomical observations	100.0
> 87	Milky Way is not visible	90.3
> 688	number of stars is drastically reduced	19.7
> 3000	extreme pollution, no stars are visible	1.3

Table 3.2: Fraction of the Italian territory under different sky brightness. Uncontaminated sites no longer exist. Adapted from *Falchi et al. (2016)*[10] [10].

Figure 3.11 shows that the most polluted areas in the country are the Padania valley in northern Italy, the Arno valley in Tuscany and the urban areas around Rome and Naples. Darkest (but still polluted) areas are in the northern Alps, the southern Apennines (Abbruzzo, Basilicata and Calabria) and central Sardinia.

Figure 3.11: Sky brightness above Italy [10].Source: www.lightpollutionmap.info.

Evolution of the LP in Italy.   First analysis of LP in Italy is by *Bertiau et al. (1973)*[2]. Using data about city population and a basic light propagation model, the authors provided a map of the Italy sky brightness with a resolution of 15 km.

Similar works have been repeated during the time by Cinzano (see for example *Cinzano (2000a)*[5]) before the introduction of the world atlas. In the figure 3.12 is shown the evolution of light pollution in Italy since the *Bertiau et al.* The prevision of the Figure, matches well with observations on the New World Atlas of Light pollution ([10]), shown in Figure 3.11, but with a slightly different color scale.
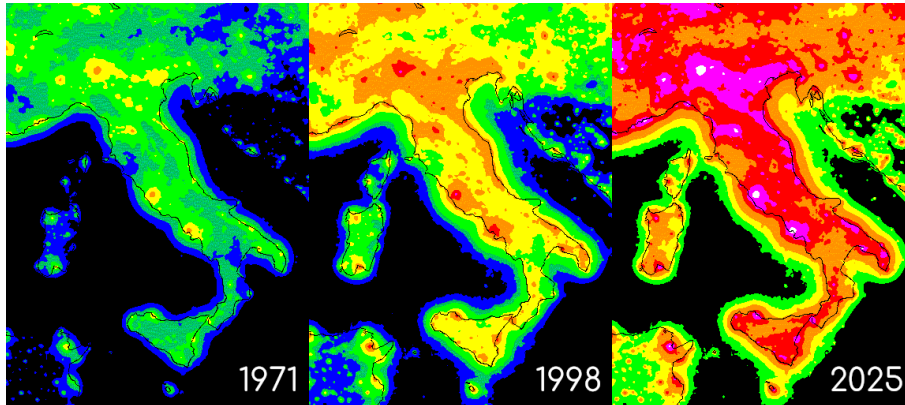
Figure 3.12: Sky brightness maps of Italy, obtained from population data, **??**. Note the constant expansion of urban areas and the reduction, till the extinction of dark sites. Based on maps by P. Cinzano, available through www.cielobuio.org.

3.5.3   In Asiago

Current situation.   The LP situation is Asiago follows the global increasing trend, observed for Italy. According to the data collected with the SQM installed at Cima Ekar [19], typical sky brightness in the visual band is around 21.7 mag/arcsec^2 corresponding to 230 μcd m^{-2}.

Evolution of LP in Asiago.   In *Cinzano (2000b)*[6] are collected historical photometric observations carried out in Asiago between 1960 and 1995. According to the results of the study the sky brightness in these years had an exponential growth with an annual rate of increase of about 10%. In Figure 3.13 are reported the results of the study.
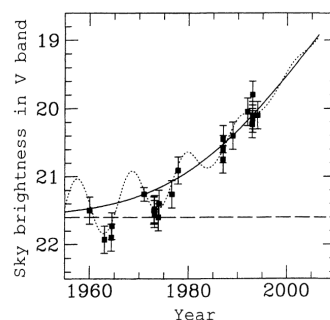
Figure 3.13: Sky brightness in the V band from Asiago, between 1960 and 1995. Best fit curve is the solid line, while the dotted one represents the correction for solar activity effects. From *Cinzano (2000b)*[6].

Chapter 4

Sky spectra reduction

In this chapter are reported the steps in the data reduction that I designed to extract spectra of the sky from frames originally taken for scientific purposes. After a brief overview I describe accurately the data reduction process that I built. To improve the readability of this writing, I will report only the most significant pieces of code. The complete scripts and all the analysis results are available under a GitHub repository at the page `https://github.com/codatomrc/tesi`.

4.1 Introduction

4.1.1 Software management and reduction steps

In this work I developed some pieces of Python (v. 3.10) code to manage all the steps of the data reduction. Note that most of the data pre-reduction was already done and was not necessary to use old software such as IRAF or its Python version PyRAF. In this work I tried to heavily automatize the script in order to be able to analyze all the frames with a single run. Many efforts were spent to build a robust code, capable of working correctly for spectra with very different features, without the necessity to fine-tune the software settings every single time a new frame is processed. All of this effort was made in order to be eventually able, in the future, to rapidly analyze new frames.

I decided to divide the source code into two independent main scripts, each one devoted to a specific task. It follows a brief description of each step of the data reduction process.

Background extraction Starting from the original spectra I have to separate the scientific targets from the background (bkg) regions. Once identified the spectra of the targets and cosmic rays, the relative regions are masked. The remaining area contains the spectrum from the sky bkg only which is extracted to a new file.

Background analysis The sky spectrum is averaged along the slit direction. From the regions that do not present lines is estimated the shape of the sky continuum emission. Prominent lines or lines of interest are identified and the relative equivalent width is computed. The output of bkg analysis is the estimation of the continuum emission and the list of the widths of the emission lines.

4.1.2 The dataset

This work is based on 35 spectra taken between 2006 and 2021 in the Osservatorio Astrofisico di Asiago, Asiago, northern Italy. Spectra were obtained by Professor Stefano Ciroi and collaborators to collect data on studied astronomical objects and were taken with the 1.22 m reflective telescope "Galileo Galilei" equipped with the grating spectrograph "Boller & Chivens".

Each frame has been pre-reduced by Ciroi and its work group: data has been corrected for bias and flat field and calibration on both flux and wavelength was performed; Table 4.1 contains relevant information of each file. Cosmic rays were not removed as well as the sky bkg. Before November 2011 frames had a spatial scale on the CCD of 0.63 arcsec/px while on later data the scale was 1.0 arcsec/px. For all the objects, grating with a line density of 300 tr/mm was used while the grating angle varied between 0° and 5.25° according to the type of target. Similarly slit aperture size varied from a minimum of 200 to a maximum of 400 μm while the exposure times ranged between 300 and 3600 s.

filename (**.fits)	date yyyy-mm-dd	time UTC	name ID	exposure time [s]	slit size [μm]	airmass
ima_010	2006-02-17	N.A.	NGC2392	600.0	250	1.186
ima_015	2006-10-24	N.A.	Ark564	1800.0	300	1.095
ima_005	2008-08-01	N.A.	kou2056	1200.0	350	1.547
ima_023	2007-05-10	N.A.	sn2007bt	1800.0	300	1.242
IMA00811	2008-09-01	20:17:56	V2491 Cyg	1800.0	250	1.029
ima_000	2008-06-27	N.A.	V0458 Vul	1200.0	250	1.115
ima_001	2008-04-05	N.A.	CGCG008-077	1800.0	300	2.426
IMA03582	2009-02-25	20:56:09	kw 97 27-49	1200.0	250	1.241
IMA05127	2009-07-25	21:33:40	[KW97] 36-10	1200.0	250	1.574
IMA06889	2009-09-27	01:11:50	SN2009ig	1800.0	250	1.472
IMA08828	2010-03-06	18:12:15	ngc 660	1200.0	250	1.349
IMA08888	2010-03-06	23:06:46	ngc3079	1800.0	250	1.014
IMA10596	2011-02-06	23:41:35	ngc2841	1800.0	200	1.004
IMA13299	2011-11-19	00:25:26	Mrk6	1800.0	250	1.219
IMA13751	2011-12-11	01:25:40	mrk 6 PA=30	1800.0	250	1.141
SCR02491	2011-09-18	21:51:26	HR Del	1200.0	300	1.125
IMA15544	2012-01-21	23:27:55	NGC3516	1200.0	300	1.268
IMA19211	2012-03-21	23:16:50	Mrk6 PA-40	1800.0	200	1.357
IMA22652	2012-07-11	21:31:00	PKS 1424+240	1200.0	350	1.359
IMA25484	2012-10-26	02:05:51	MRK3 PA=20	900.0	250	1.118
IMA27818	2013-02-02	18:04:23	mrk 3 pa-sky 110	1200.0	200	1.175
IMA39753	2016-05-31	22:41:37	M57-slice1	180.0	300	1.067
IMA53190	2018-10-13	01:04:03	IC 3599	1200.0	400	1.144
IMA53906	2016-03-31	02:07:25	3C279	1200.0	300	1.756
IMA61434	2017-01-31	22:19:40	k1808	300.0	200	1.257
IMA68006	2017-11-24	00:17:04	KW97 16-54	300.0	200	1.025
IMA70536	2018-04-08	22:35:04	IC3599	600.0	250	1.062
SCR01731	2019-04-03	23:41:23	3c273	600.0	200	1.393
IMA84983	2020-05-17	20:50:05	S5 1027+74	900.0	300	1.15
IMA88753	2020-11-08	21:06:29	4FGL_J0152	600.0	300	1.428
IMA91077	2020-12-18	20:34:15	4FGL_J0710	600.0	300	1.293
IMA100558	2021-11-10	01:43:18	3C 120	1200.0	200	1.369
IMA95725	2021-06-01	21:17:36	AGN_ign_194.71_23.92	900.0	250	1.156
IMA97134	2021-07-11	21:37:36	4FGL J1725.0+1152	900.0	250	1.207

Table 4.1: A synthesis of the main properties of the files in my dataset.

4.1.3 Known sky lines

In Table 4.2 I reported a list of the possible lines visible in the night sky spectrum of a polluted site. Most of the lines come from Mercury and Sodium vapor lamps that contain traces of other elements, such as Li and Sc respectively. The few remaining identified transitions come from the natural airglow, see 2.2 A special case is the Na doublet $\lambda 5890, 5896$ which is produced both from airglow and Sodium vapor lamps.

Most of the lines in the table have been identified by S. Ciroi using a high resolution spectrum of the night sky in Asiago (*Ciroi*, private communication). I further extended the list with lines identified by *Slanger et al. (2003)*[23], *Sanchez et al. (2007)*[21] and *Zhang et al. (2016)*[26]. Note most of these lines are very faint in the spectra available and only a restricted fraction of them has been used in the analysis (see 5.2.1).

4.2 Background extraction

Data available were not taken with the aim of monitoring the sky conditions and contain astronomical objects. The first step in the data reduction is to identify the regions of the spectra where there are the scientific targets. Most of the effort described below is to automate the process.

wavelength (Å)	origin	notes
4046.56	HgI	
4077.84	HgI	
4100.32	ScI	[23]
4163.59	NeI	[23]
4358.34	HgI	
4420.	NaI	[26]
4423.	NaI	[26]
4511.37	ScI	+5 ScI lines
4664.81	NaI	
4668.56	NaI	
4670.83	HgI	+ScI
4753.17	ScI	+NaI
4827.	HgI	[26]
4832.	HgI	[26]
4916.07	HgI	[23]
4978.54	NaI	+ScI, HgI
4982.81	NaI	+ScI, HgI
5085.0	ScI	[23]
5148.84	NaI	
5153.40	NaI	
5156.99	ScI	
5199.	NI	N,[26]

wavelength (Å)	origin	notes
5349.71	ScI	
5354.03	HgI	
5355.79	ScI	
5356.10	ScI	
5372.36	ScI	[23]
5418.02	XeI	
5460.75	HgI	
5577.34	[OI]	N
5668.75	ScI	
5671.83	ScI	
5675.81	HgI	
5682.63	NaI	+XeI
5688.21	NaI	+XeI
5769.61	HgI	
5790.67	HgI	
5889.95	NaI	N
5895.92	NaI	N
6113.47	ArI	CFL
6154.23	NaI	
6160.75	NaI	
6230.0	OH	N,[26]
6300.30	[OI]	N
6708.	LiI	[21]

Table 4.2: Brightest artificial and natural spectral lines (those marked as "N" in the notes column).

On Figure 4.1 is shown as an example the spectrum of the active galaxy labeled 4FGL J0512 (file `IMA88753.fc.fits`). Two main astronomical sources are visible as long strips in the top and bottom side of the frame. The other bright vertical lines and bands represent the emission of the sky diffuse bkg. Looking carefully some cosmic rays can be also spotted toward bluer wavelengths. This frame will be used later to show the different steps in the data processing.
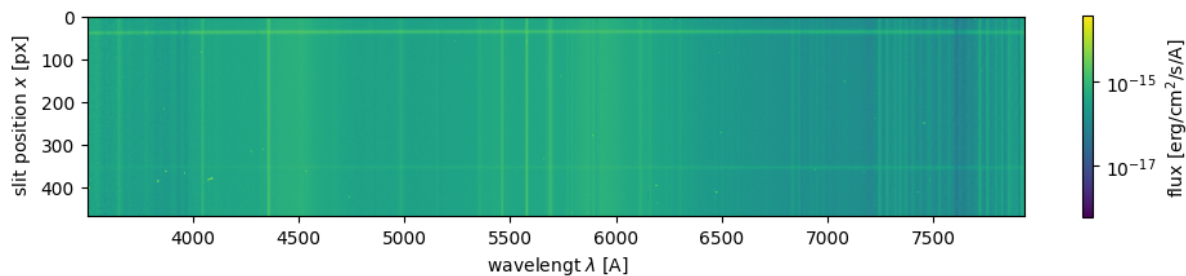
Figure 4.1: An example spectrum from the dataset. The frame `IMA88753.fc.fits` contains the active galaxy "4FGL J0152". Main components are the galaxy and another source (horizontal stripes), the diffuse bkg (vertical lines and bands) and some cosmic rays (especially below 4000 Å).

4.2.1 Preamble

Before the actual data analysis I need to load all the necessary.

Modules, options and parameters. First I need to load packages and set parameters to allow the rest of the script to work correctly.

```
import numpy as np
import matplotlib.pyplot as plt
from matplotlib import colors
from astropy.io import fits
```

```python
from scipy.signal import find_peaks, peak_widths
from datetime import datetime
import glob
import os
from wotan import flatten


#########################
#OPTIONS
save_plots = True
save_FITS = True
plot_profile = True
plot_spec = True
show_ima = True


#PARAMS
peak_height = 0.05 #height above the bkg level
data_col_frac = .75 #minimum fraction of valid pixels in a column
width_mult = 2 # interval to exclude around a source, wrt center in FWHM units
cr_width = 2.5 # cr trace spatial width
cr_prominence = 5 #threshold height wrt average column level
cr_pad = 1 # number of px to exclude around cr, in a fixed column
LAMBDA_lim = 40000 #A, limit blue wavelength
#########################
```

Options are some special parameters that allow to enable or disable some debugging diagnostics useful in the development phase. Parameters are some special values that can be changed to control the final output result. Each of these lines will be explained later when appearing in the code.

Data import and handling. Each spectrum is stored in a `.fits` file (acronym of Flexible Image Transport System, [20]). For this work I need both the actual spectrum data and the auxiliary information about the acquisition and reduction processes, contained in the header section.

To automate the process of data import I used the `glob` function from the homonyms module[1] to identify all the files with the FITS extension in a given path directory. I also needed the function `basename` from the `os.path` module[2] to retrieve the actual name of each file, since `glob.glob` provides only the full path of the files. Then the file research is implemented with the following code.

```python
#browse all the *.fc.fits files in a directory and its subdirectories
main_path = './Asiago_nightsky/'
file_ls = glob.glob(main_path+'/**/*.fc.fits', recursive= True)
names = [os.path.basename(x) for x in file_ls]

#import table of known lines
lines = np.genfromtxt('lines.txt', usecols=0)
```

`main_path` can be eventually adapted to scan new files in different directories. The choice to search for files that ends with `.fc.fits` is due to the fact that Ciroi and collaborators use the convention to append the suffixes "f" and "c" to indicate frames corrected for flat field and calibrated respectively.

4.2.2   Data extraction

For each file found in the `main_path` directory I need to extract the information contained both in the header and the data unit(s). This task is performed by the `astropy.fits.io` module and is implemented in the following way:

```python
#process all the files found
for name,file in zip(names,file_ls):

    #open a FITS file
    hdul = fits.open(file)
    hdr = hdul[0].header
```

The header is managed as a Python dictionary from which I can extract the quantities that I will need as new variables.

---

[1] https://docs.python.org/3/library/glob.html
[2] https://docs.python.org/3/library/os.html

Wavelength data. The first thing to extract is the wavelength information in the following way.

```
 #extract wavelength information from the header
NAXIS1, NAXIS2 = hdr['NAXIS1'], hdr['NAXIS2']
LAMBDA0, DELTA = hdr['CRVAL1'], hdr['CDELT1']

#generate the lambdas array
if hdr['CTYPE1'] != 'LINEAR':
    print('WARNING: no linear wavelength calibration')
LAMBDA = np.arange(LAMBDA0, LAMBDA0+NAXIS1*DELTA, DELTA)
if len(LAMBDA) == NAXIS1+1:
    LAMBDA = LAMBDA[:-1]

#remove extreme blue wavelengths
LAMBDA_start_id = len(LAMBDA)-len(LAMBDA[ LAMBDA>LAMBDA_lim])
LAMBDA = LAMBDA[LAMBDA_start_id:]
```

In this way the array `LAMBDA` contains the wavelength associated to each column of the spectrum, assuming a linear calibration. In the case the original calibration is not linear, a warning message is printed.

I decided to limit the wavelengths in the blue hand of the spectrum to the limit value `LAMBDA_lim` which was set to 4000 Å. Below this threshold the signal tends to be too noisy and low quality, due to the strong correction in the flux calibration phase and the intrinsic low sensitivity of CCDs in the blue domain. Also `LAMBDA_lim` is meant to be a parameter that can eventually be changed to fit new data.

In Figure 4.2 is show the bluest hand of the spectrum of the planetary nebula NGC2392 (also known as "The Eskimo nebula"), taken on the 1 February 2006: the signal is extremely noisy due to the extreme calibration necessary at those wavelengths. Note also the presence of several cosmic rays (red circles) that provide further spurious signals to the spectrum.
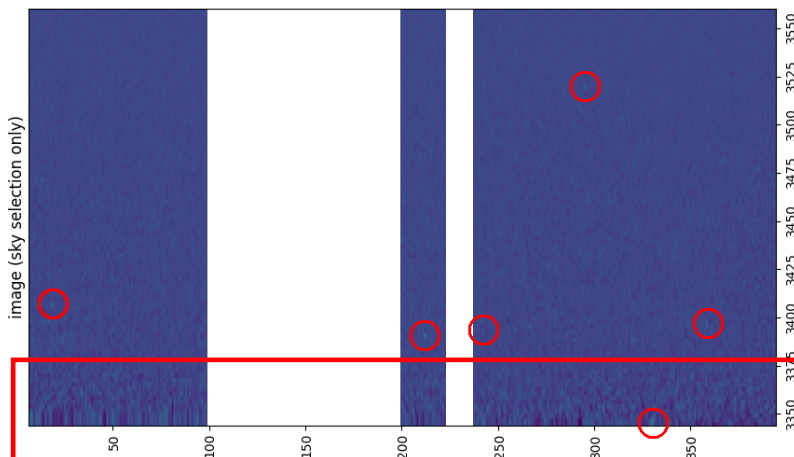

Figure 4.2: Extreme blue/UV domain in the spectrum of the nebula NGC2392. The area in the rectangle is totally useless due to the noise. Cosmic rays have been highlighted too.

Slit and scale data. Before 2008 the format of the saved files was slightly different from the current standard: in the header of the files some entries had different names and others did not exist. For my purposes I have to specify by hand the entries for the angular scale on the focal plane of the telescope (the parameter `TELSCALE`) and the scale on the detector (labeled as `CCDSCALE`), that are not recorded in the original file.

```
    year = hdr['DATE-OBS'][:4]

#add evental scale missing information in the hdr
try:
_ = hdr['TELSCALE']
except KeyError:
hdr['TELSCALE'] = 10.70 #arcsec/mm, Ciroi, private communication
hdr['CCDSCALE'] = 0.63 #arcesc/px, Ciroi, private communication
```

4.2.3 Cosmic ray and noise removal

The next step in the sky extraction process is to remove the cosmic rays and the residual noise in the blue domain. These two sources of photons provide spurious signals that may interfere with the detection and removal of the astronomical signal from the background. See for example Figure 4.2 at page 33.

Implementing an automatic process of recognition and masking of the spurious signals from cosmic rays and photon noise is rather complex and requires quite advanced analysis tools. The steps I made are the following:

1. I scan each column of the spectrum, i.e. for each fixed value of the wavelength. The average flux level of the column is computed as a reference of the brightness of the spectrum at the analyzed wavelength.

2. In each column I look for sharp peaks in the flux due to the presence of cosmic rays or strong noise. The peaks are identified with the function find_peaks[3] from the module scipy.signal[22]. In particular I restricted only to peaks with a width below the value of cr_width= 2.5 px and a prominence[4] higher than cr_prominence= 5 times the average value of the column. These are good settings to filter only peaks of noise and cosmic rays that are typically very sharp and much brighter than the astronomical signal.

3. I mask the pixels around the peaks. The number of pixels to mask is computed from the width of the peaks, which is provided by the function peak_widths [5] from scipy.signal. I used this function to compute the FWHM of each peak, since this was a more solid width estimator with respect to the full width, which may be biased due to the noise fluctuations around the peak. I assumed that the total width of the peak was $2 \times$ FWHM. To be sure all the cosmic rays traces or the noise fluctuations were contained in the detected width, I conservatively decided to increase the masked interval of a further cr_pad= 1 px in both directions along the columns.

4. I remove all the columns where too many pixels have been masked, i.e. too noisy columns. The minimum fraction of saved pixels in a column must be higher than the value data_col_frac= 0.75.

After the removal of sharp peaks and noisy columns I expect to have a clean frame which contains only the spectra of the astronomical targets and the background sky. The procedure described above is implemented by the following lines.

```
#########################
 #import data
raw_data = hdul[0].data[:,LAMBDA_start_id:]/area #brightness
raw_integr = np.sum(raw_data, axis = 1)

########################
#remove cosmic rays and UV noise
x = np.arange(len(raw_integr))
data = np.copy(raw_data)

cr_col_frac = np.zeros(len(LAMBDA)) #fraction of remaining px
for cr_col,col in enumerate(data.T):
    col_avg = np.nanmean(data[:,cr_col])
    cr_line,_ = find_peaks(col,
                   prominence = cr_prominence*col_avg,
                   width = (0,cr_width))

    cr_widths = peak_widths(col, cr_line, rel_height=0.5)[0]

    #set left and right boundaries of the source region along the slit
    left_width = cr_line-cr_widths - cr_pad
    right_width = cr_line+cr_widths + cr_pad

    #scan each column and remove peaks
    cr_sel = np.zeros(np.shape(col), dtype=bool)
    for i in range(np.shape(col)[0]):
        for peak,width in zip(cr_line,cr_widths):
            if abs(i-peak) < width+cr_pad:
                cr_sel[i] = True
```

---

[3] https://docs.scipy.org/doc/scipy/reference/generated/scipy.signal.find_peaks.html
[4] See the "Notes" section in the documentation page
[5] https://docs.scipy.org/doc/scipy/reference/generated/scipy.signal.peak_widths.html

```
    #counts how many pixels are left in a column
    saved_px = (NAXIS2 - np.sum(cr_sel))/NAXIS2
    cr_col_frac[cr_col] = saved_px
    if saved_px >= data_col_frac: #if enough, take the masked column
        data[cr_sel, cr_col] = np.nan
    else: #else discard the entire column
        data[:, cr_col] = 0.
```

4.2.4   Sources identification

The main idea to find scientific target is to integrate the (cleaned) spectrum in the wavelengths and obtain the integrated luminosity profile of the telescope field through the slit. Astronomical sources are spatially limited and thus appear as bright peaks over the flat homogeneous background. Unfortunately, in some real spectra the continuum is not homogeneous but present some gradients, probably due to some calibration biases as shown for example in Figure 4.4; consequently, the background integrated luminosity profile may not be flat at all, complicating the detection of astronomical signals. If $F(x)$ is the total luminosity profile, we can imagine to split the two components

$$F(x) = A(x) + B(x) \tag{4.1}$$

where A is the signal due to the astronomical sources and B the one from the background.

The full implementation of the identification process follows the steps below:

1. Integrate the spectrum along the wavelengths to retrieve the luminosity profile along the slit. Estimate the typical luminosity value of each profile as the median one; median value is much less sensitive to peaks in the luminosity profile and for this reason is preferable with respect to other estimations such as the average.

   If $F(x, \lambda)$ is the flux in a pixel of the spectrum in the position x along the slit and wavelength λ, then the luminosity profile $F(x)$ is obtained as

   $$F(x) = \int_{\lambda_{min}}^{\lambda_{max}} F(x, \lambda') \mathrm{d}\lambda' \tag{4.2}$$

   while typical luminosity value is

   $$\hat{F} = \operatorname*{median}_{x} \{F(x)\} \tag{4.3}$$

2. Estimate the general trend of the background B, i.e. regardless of the presence of peaks of the astronomical targets. I used the function `flatten`[6] from the `wotam` package [15] to perform a bi-weighted detrending of the signal. This technique consists of estimating the smoothened value of the signal in the position x as the median value of the data centered in x and a window of total span w. A more robust indicator is obtained when data are filtered such that points with a larger displacement to the median value are less relevant. Given the value of the residual a of the data with respect to the median value, there can be several different types of relative weight functions; in the wotam package it is used the Tukey function which is expressed as

   $$L(a) = \begin{cases} \left[- \left(\frac{a}{c}\right)^2 \right]^2 & \text{if } |a| < c \\ 0 & \text{else} \end{cases} \tag{4.4}$$

   where c is a tuning parameter that specifies the steepness of the weight scale.

   I used a windowing of 50% the total profile length and a fine-tuning parameter `cval`$= c = 10$. Such a large window can only partially smooth down the peaks signals. Called $\mathcal{S}_{w,c}$ the bi-weighted filter operator, with window w and tuning parameter c then the smoothed luminosity profile is given by

   $$F'(x) = S_{w,c}\{F(x)\} = \operatorname*{median}_{x \pm w} [F(x)] \, L \left(\left| F(x) - \operatorname*{median}_{x \pm w} [F(x)] \right| \right) \tag{4.5}$$

---

[6]`https://pypi.org/project/wotan/`

3. A better approximation for the background B can be obtained by masking the data around the astronomical sources. I used as threshold the detrended profile F', vertically shifted by a factor equal to the 5% of the average bkg level $\hat{F}$. The new profile obtained is

$$F''(x) = F'(x) \cdot \theta(x) \qquad \text{where} \quad \theta(x) = \begin{cases} 1 & \text{if} \quad F(x) \leq F'(x) + 0.05 \cdot \hat{F} \\ \text{nan} & \text{else} \end{cases} \tag{4.6}$$

The new masked profile F'' is much closer to B than the original profile as the contribution of astronomical sources A has been drastically decreased.

4. The final background profile estimation is obtained by a further filtering of the masked trend F''. I used the `flatten` function with a window of 10% the profile length. This allows to smooth the noise fluctuations in the background. Formally

$$B(x) \approx S_{W,c}\{F''(x)\} \tag{4.7}$$

where $W \ll w$ is the new windowing factor, while the value c has been kept constant. Once estimated B, I can focus on the profile of the astronomical sources A which can be isolated simply as $A = F - B$.

In Figure 4.3 are plotted the various luminosity profiles used to retrieve the final background B in my example frame (see above). In this case the background is quite constant along the slit and the signal from the sources stands out the background easily; even the preliminary filtered profile F' would have been a good approximation of the background, without the necessity of further computation, which is instead necessary for frames with lower quality data, as reported for example in Figure 4.4 with the file `IMA91077`.
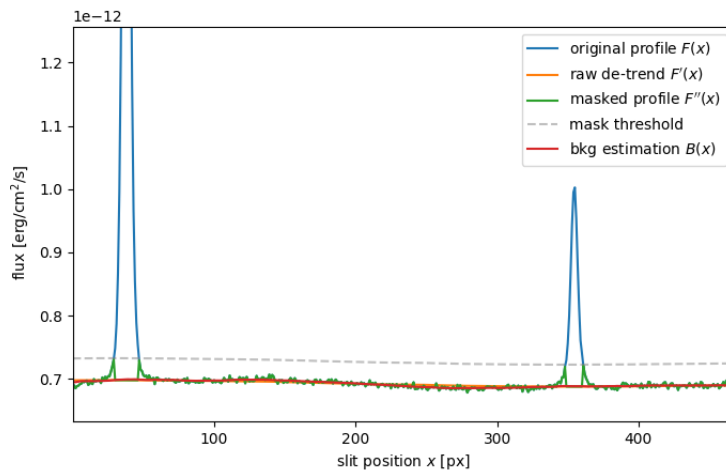

Figure 4.3: Estimation of the background B on my test frame. Thanks to the good quality of the data (uniform slit illumination, high signal-to-noise ratio) the identification of the sources is particularly easy.

5. Identify the peaks in the profile of the astronomical sources A with the function `find_peaks` (see above). I selected peaks higher than 4% of the reference level $\hat{F}$ and broader than `cr_width`; the first condition ensures not to include faint peaks due to background noise fluctuations, the second one, prevents from including sharp peaks produced by cosmic rays.

6. Estimate the width of the peaks with `peak_widths` that provided the FWHM. Many astronomical sources such as galaxies or planetary nebulae present a bright core and faint extended wings. This means that the FWHM can underestimate the total width of a peak if wings are very broad. In a conservative approach I decided to assume the peak width as $2 \times$ `width_mult` $\times$ FWHM where `width_mult` $= 2$ is another tunable parameter of the script. With the resulting widths I masked the regions centered around the peaks.

In Figure 4.5 are shown the areas associated with the astronomical sources that have been removed, in my example frame (red bands) and the final background signal (greed dots).
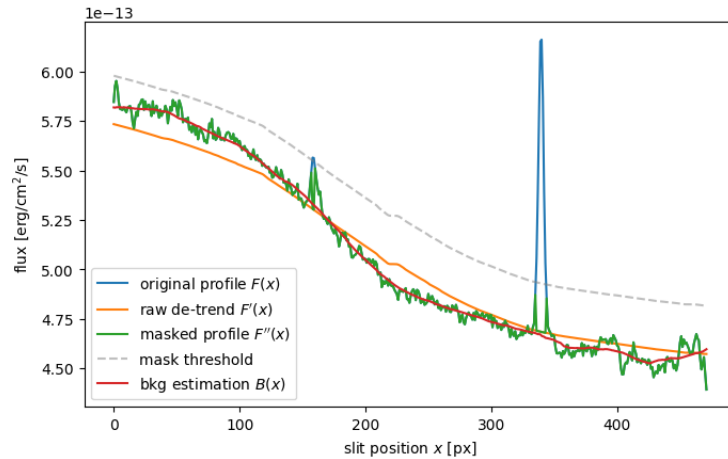
Figure 4.4: Estimation of the background B on my test frame. Due to the bad quality of the data the estimation of the bkg is much more complicated and requires more analysis steps.
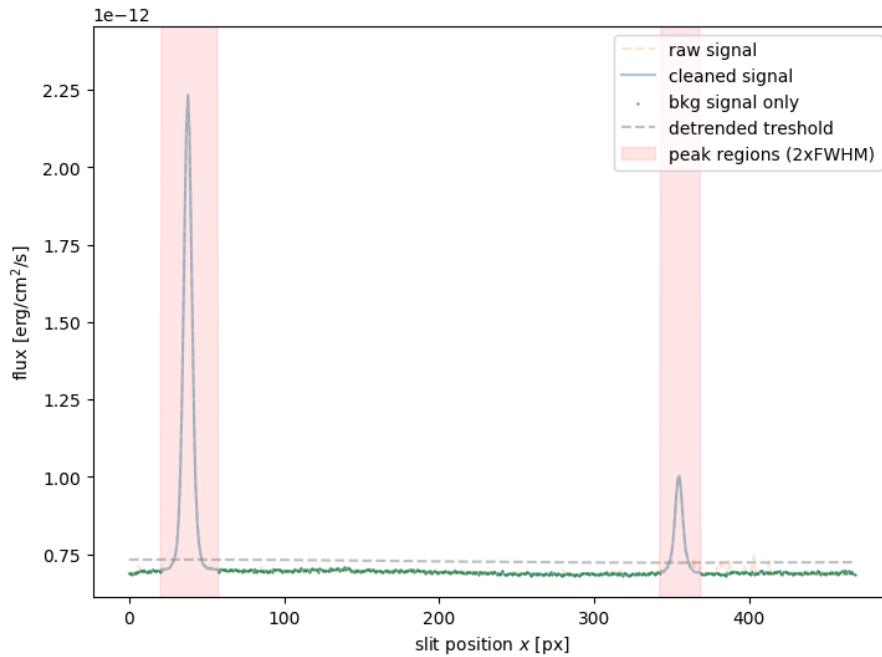

Figure 4.5: The astronomical sources identified by the script in the test frame. The original profile (broken orange line) has been filtered to remove cosmic rays and noise, contributing to smooth out the profile into the cleaned one (light blue solid line). Red areas on the cleaned profile are the regions occupied by the sources and are going to be masked. The remaining usable signal from the background is represented by the green dots, each one representing a row in the bidimensional spectrum.

The masked intervals in the luminosity profiles became masked rows, when back to the bidimensional spectrum, which should now have only counts from the sky background.

On Figure 4.6 is finally reported the background sky spectrum extracted from the example frame. The white areas have been masked due to the presence of astronomical sources or cosmic rays.

The full code to implement source extraction is the following.

```
#use noise/bkg info to find peaks
integr = np.nansum(data, axis = 1)
bkg_est = np.median(integr)
```
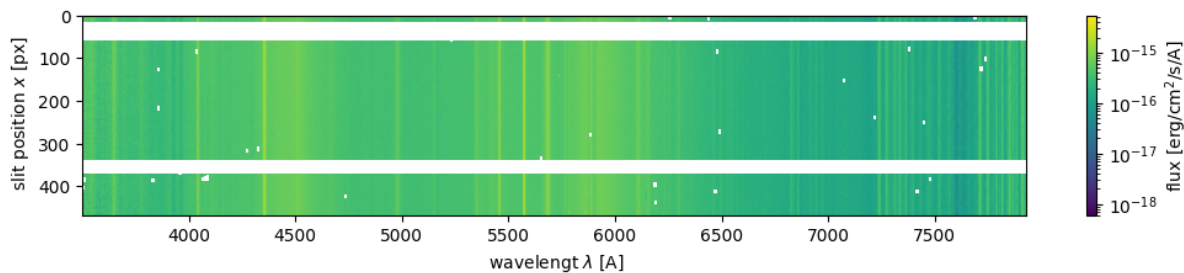
Figure 4.6: Final background spectrum extracted from the example frame.

```python
#detrend: global trend (including peaks)
_,trend_raw = flatten (x, integr ,
                       method ='biweight',
                          window_length =0.5*NAXIS2 ,
                       cval = 10, return_trend = True )

#trim removing peaks, i.e. data fare above the global trend
integr_trim = np.where(integr <= trend_raw+0.04*bkg_est ,
                       integr , trend_raw)

#detrend the trimmed data, much less sensitive to the peaks
_,trend = flatten (x,
                   integr_trim ,
                   method ='biweight',
                   window_length =NAXIS/10. ,
                   cval = 10, return_trend = True )

#detrend residuals: original peaks are highlighted wrt the bkg profile
diff = integr-trend

#find peaks
peaks,properties = find_peaks(diff , height =0.04*bkg_est , width = cr_width)
peak_FWHM = peak_widths(integr , peaks , rel_height=.5)[0]/2.

if len(peak_FWHM)== 0:
print( " WARNING: no sources were detected")

#generate a boolean mask True outside the peaks
bkg_sel = np.full(np.shape(x), True)
for i,peak in enumerate(peaks):
    width = (int(peak_FWHM[i])+1)*width_mult
    for w in range(-width,width):
       bkg_sel[peak+w]=False
    w = width -1
    while integr[peak+w] >= trend[peak+w]:
       bkg_sel[peak+w] = False
       w += 1
    w = width
    while integr[peak-w] >=trend[peak-w]:
       bkg_sel[peak-w]=False
       w += 1

#########################
#integrated spectrum (along the slit)
total = np.nanmean(data, axis = 0) #integration along the slit
sky = np.nanmean(data[bkg_sel ,:], axis = 0) #integration of bkg rows only

total[total == 0] = np.nan

#########################
#extract only the bkg rows

ma_data = data #set masked data
for i,row in enumerate(bkg_sel):
    #cancel data from the source rows
    if row == 0:
       ma_data[i,:] = np.nan
```

4.2.5   Sky spectrum export

Once masked all the contaminants, I can extract the sky spectrum and save it for further analysis. For each frame I create a new `.fits` file that contain the sky spectrum and the masked data from other sources. The header of the new file contain the same information of the original one, plus further further additional information about the time of creation and the value of the limited wavelength `LAMBDA_lim` (respectively "BKGEXTR" and "UVLIM"). Each file is saved in the same directory of the original one and to its name is appended the `.bkg.` suffix.

```python
#########################
#save masked data in a new FITS file
if 1 == save_FITS:
    now = datetime.now()
    now_str = now.strftime("%Y-%m-%d %H:%M:%S")

    hdr.set('BKGEXTR', now_str, 'Time of bkg extraction')
    hdr.set('UVLIM', LAMBDA_lim, 'A')
    hdr['NAXIS1']=len(data[0])
    hdr['BUNIT'] = 'erg/cm2/s/A/arcsec2'
    new_hdu = fits.PrimaryHDU(ma_data)
    new_hdul = fits.HDUList([new_hdu])
    new_hdul[0].header = hdr

    file_new = file[:-5]+'.bkg.fits'
    new_hdul.writeto(file_new, overwrite=True)
```

4.3   Background analysis

The analysis of the regions of the spectra that contain only sky is done by a separate script. The data required to work is the following:

- The sky background spectra, obtained from the previous script.

- A list of emission lines to be analyzed.

- A list of spectral regions where no lines are present. This is used to sample the profile of the continuum.

As an output of the analysis the pipeline provides estimates for:

- The equivalent width of the lines in input and relative uncertainty.

- The smoothened shape of the spectrum continuum.

4.3.1   Preamble

Before processing the data I have to call the required modules, specify parameters and options and import scientific data.

Modules, parameters and options.   It follows the very first part of the code:

```python
#########################
import numpy as np
import matplotlib.pyplot as plt
from scipy.signal import find_peaks, peak_widths
from scipy.interpolate import interp1d
from astropy.io import fits
from astropy.modeling import models,fitting
from astropy.table import Table
from datetime import datetime
import glob
import os
from wotan import flatten
#########################
#OPTIONS

plot_fits = True
save_fits = False
```

```
show_cont = True
save_cont = False

FITS_lines = False
#PARAMS
fit_error = 2 #% minimum FWHM relative error (lower hints singular/degenerate results)
fit_window = 10 # A,  semi amplitude of the fitting interval around each line
line_window = 10 #DELTA units when finding lines to be masked to estimate continuum
#########################

def line_id(array, value):
    x0=array[0]
    delta_x = array[1]-array[0]
    i = (value-x0)/delta_x
    return int(i)
```

Note I build the small function `line_id` that, given a wavelength value, returns the corresponding index in the wavelengths array.

Data selection.   The information required to run the script is obtained with the following code.

```
# import lines table
lines_raw = np.genfromtxt('lines.txt', usecols=0)
line_diff = np.diff(lines_raw)

#import spectral ranges for continuum estimation
ranges2 = np.genfromtxt('ranges2.txt')

#browse all the *.fc.fits files in a directory and its subdirectories
main_path = './Asiago_nightsky/'
file_ls = glob.glob(main_path+'/**/*.fc.bkg.fits', recursive= True)
names = [os.path.basename(x) for x in file_ls]
```

Recall that in this case the sky spectrum file has been marked with the further suffix `.bkg.` to distinguish them from the original version.

4.3.2   Data import

Wavelength calibration.   Analogously to the previous script, I have to import data in such a way that Python can manage them. I extract from the header the wavelength and angular scale of the spectra. The code is the following:

```
#process all the files found
file_id = 0
JDs = []
for name,file in zip(names,file_ls):

    #load the frame
    hdul = fits.open(file)
    hdr, data = hdul[0].header, hdul[0].data

    #take wavelength info from the hdr
    NAXIS1, NAXIS2 = hdr['NAXIS1'], hdr['NAXIS2']
    LAMBDA0, DELTA = hdr['CRVAL1'], hdr['CDELT1']
    LAMBDA_lim = hdr['UVLIM']
    year = hdr['DATE-OBS'][:4]
    JDs.append(hdr['JD'])
    TELSCALE, CCDSCALE = hdr['TELSCALE'], hdr['CCDSCALE']

    slit = hdr['SLIT']/1000.*TELSCALE/CCDSCALE #px

    #the (eventually) UV-limited wavelengths array
    LAMBDA_start = max(LAMBDA_lim, LAMBDA0)
    LAMBDA = np.arange(LAMBDA_start, LAMBDA_start+NAXIS1*DELTA, DELTA)
    if len(LAMBDA) == NAXIS1+1:
        LAMBDA = LAMBDA[:-1]
```

Blended lines management.   The spectra in my dataset present a relatively low resolution and some lines that are too close and get blended on each other, making actually a single spectra feature. To avoid

repetitions in the analysis, when a group of close lines is met, the pipeline considers only the first line and discards the others. The code to "simplify" groups of close blended lines is the following:

```python
spec = np.nanmean(data, axis=0) #in energy count units erg/cm^2/s/A

#remove blended lines, i.e. to be considered as a single feature
close_lines = np.where(line_diff < slit*DELTA, False, True)
close_lines = np.insert(close_lines, 0, True)
lines = lines_raw[close_lines]
```

As a selection threshold I used the width of the slit projected on the detector expressed in wavelength units.

4.3.3 Continuum estimation

One of the most challenging parts of the script is to develop a solid way to automatically extract the shape of the continuum component of the spectrum, below the emission lines. The main challenge for this process is to find the proper way to automatically identify the characteristic spectral features of the continuum and at the same time ignore the contributions from the emission lines. The best solution turned out to be performing a sampling of the continuum emission in appropriate regions of the spectrum.
    Let us see in detail how the continuum extraction is implemented:

1. Determine a list of sampling regions of the spectrum with the following requisites:

    - do not contain emission lines,
    - are distributed in such a way to sample all the relevant features of the continuum,
    - are small enough to approximate the continuum as constant in the interval.

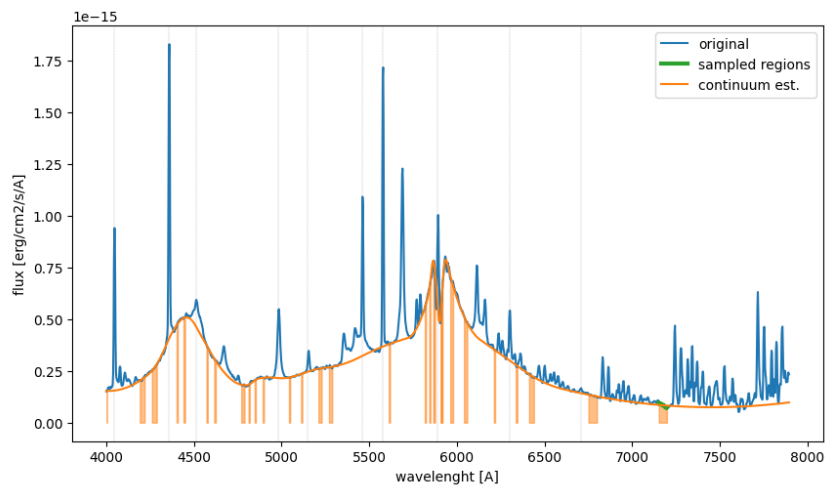   In Figure 4.7 are reported the sampling regions used.

Figure 4.7: The sky spectrum extracted from the test frame (solid blue), the estimation of the continuum (solid orange) and the sampling regions used to determine it (orange bands).

2. To mitigate the noise effects on the single sampling region I consider as sampled value for the signal its average in the region. If the region is small enough this is a good approximation. As sampled wavelength I use the mid-value of the region considered. In this way I have a set of sampling values (pairs wavelength-flux) for the continuum.

3. I interpolate the continuum using the sampled values over all the spectrum wavelengths. In particular I used a quadratic spline implemented by the function `interp1d`[7] of the module `scipy.interpolate`.

The Python code to implement the interpolation is the following.

---

[7]`https://docs.scipy.org/doc/scipy/reference/generated/scipy.interpolate.interp1d.htm`

```
########################
#CONTINUUM ESTIMATION

cont_sample = np.zeros(len(LAMBDA)) #samples array

x,y=[],[]
plt.plot(LAMBDA, spec, label='original') if show_cont else 0
#iterate over the sampling intervals
for Range in ranges2:

    #LAMBDAs in the sampling ranges
    in_range = (LAMBDA > Range[0]) & (LAMBDA < Range[1])
    if np.sum(in_range) == 0:
        print(f'WARNING: no data in the interval from {Range[0]}A!')


    #average the signal (small interval, contant approx.)
    LAMBDA_avg = np.mean(LAMBDA[in_range])
    spec_avg = np.mean(spec[in_range])

    x.append(LAMBDA_avg)
    y.append(spec_avg)

#interpolate the continuum from the sampling intervals
interp = interp1d(x, y, kind = 'quadratic', fill_value="extrapolate")
final_cont = interp(LAMBDA)
```

4.3.4   Line width measure

In this work I quantify the width of the lines by using the equivalent width (EW), which in this case I defined as

$$\text{EW} = \int_\lambda \frac{F(\lambda) - F_0(\lambda)}{F_0(\lambda)} \mathrm{d}\lambda \tag{4.8}$$

where F represents the signal of the line while F_0 is the level of the underlying continuum. Note the traditional definition of EW implies that absorption lines have positive values while emission lines have negative widths. Since in this work I deal with emission lines only, in order to avoid carrying a minus sign over all the work, I decided to invert the sign of the orginal definition and work with positive EW values.

When considering emission lines on my spectra, it turns out that many of them are partially overlapping in their tails. This prevents us from directly computing the EW straightly using equation (4.8). To solve this issue I developed the following procedure

1. Fit each single line only in the region close to its center, i.e. do not consider the tails that may eventually overlap with each other.

2. Fit each line with a Lorentz profile, as it proved to be closer to the actual line shape with respect to Gaussian or any other profiles. Line profile was modeled with the function `Lorentz1D`[8] from the `astropy.modeling.models` module [1]. The fit was performed with the optimized function `LevMarLSQFitter`[9] from the module `astropy.modeling.fitting`.

3. Compute the EW using the best fit profile for each single line instead of the actual signal around such line. A correctly fitted profile asymptotically tends to zero, so I could integrate it over all the available wavelengths. This method allows to somehow deblend groups of partially overlapping lines.

4. Estimate the uncertainty on the EW using the one from the fit. Let σ_{FWHM} be the variance on the best fit FWHM: assuming lines have all the same shape, then $\text{FWHM} = k\text{EW}$ where k is a fixed numeric constant. According to the error propagation theory, an estimator of the uncertainty on the EW is simply

$$\sigma_{\text{EW}} = \frac{\sigma_{\text{FWHM}}}{\text{FWHM}} \cdot \text{EW} \tag{4.9}$$

   Note this is an approximate indicator, obtained from the fit in a restricted region of the signal and not accounting for other eventual uncertainty sources, such as for example, the one on the continuum estimation.

---

[8]`https://docs.astropy.org/en/stable/modeling/models.html`
[9]`https://docs.astropy.org/en/stable/api/astropy.modeling.fitting.LevMarLSQFitter.html`

The result of the fit of some example lines on the test frame is shown in Figure 4.8. The procedure allows us to fit both isolated lines, like the $\lambda 4979, 4983$ Na dobluet (considered as a single line due to the vicinity and low spectral resolution, see above), as well as partially blended ones, like the $\lambda 5461$ Hg line.
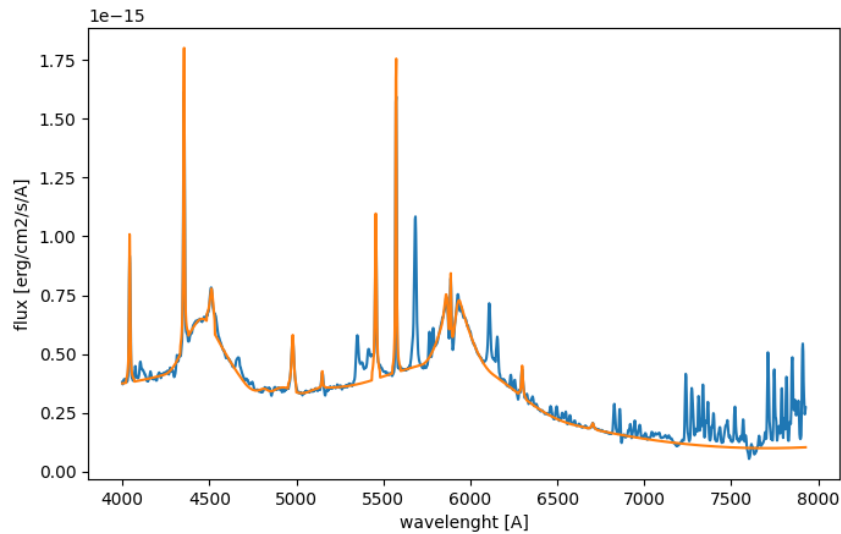

Figure 4.8: The sky spectrum extracted from the test frame (solid blue) and the best fit profiles of some test lines, overlapped to the estimated continuum. The procedure can fit both isolated and partially overlapped lines.

It follows the line fitting code.

```
#####################
#LINE FIT
EWs = []
EW_errors = []

for line in lines:

    #set fit window
    center = line_id(LAMBDA, line)
    fit_range = np.zeros(len(LAMBDA), dtype=bool)
    fit_range[center-fit_window:center+fit_window] = 1

    #prepare the model
    V =  models.Lorentz1D(amplitude=0.5*max(spec),
                          x_0=line, fwhm=10.)
    fit = fitting.LevMarLSQFitter()
    y_data = spec-final_cont

    #perform the fit and get the width
    line_fit = fit(V, LAMBDA[fit_range], y_data[fit_range],maxiter=1000)
    width_error = np.sqrt(fit.fit_info['param_cov'][2,2])/line_fit.fwhm.value

    #remove negative or singular results
    if width_error <= fit_error/100.:
    width_error = np.nan


    #compute EW
    EW = np.sum(line_fit(LAMBDA)/C/final_cont)
    EWs.append(EW)
    EW_errors.append(EW*width_error)

    #attribute the same EW to each component os blended lines
    EW_array = np.zeros(np.shape(lines_raw))
    EW_array[~close_lines] = np.nan #grouped lines
    EW_array[close_lines] = EWs

    #same for the error
    EW_error = np.zeros(np.shape(lines_raw))
```

```
EW_error[~close_lines] = np.nan #grouped lines
EW_error[close_lines] = EW_errors

for i,EW in enumerate(EW_array):
if np.isnan(EW):
    EW_array[i] = EW_array[i-1]
    EW_error[i] = EW_error[i-1]
```

4.3.5 Natural lines zenit intensity correction

As discussed in Chapter 2, intensity of airglow lines is significantly related to factors such as the observing zenital distance and the solar activity Moreover, they are affected by significant extinction due to the large geometrical depth between the observer and the atmospheric emitting layers.

As discussed in the equation (2.2) at page 13, the intensity of airglow increases towards the horizon due to the increasing of the geometrical depth of the emitting layer. At low zenit angles the relation between atmospheric extinction and observing zenit distance can be considered as a constant, i.e. extinction affects observations only close to the horizon. Under such assumptions I can correct the intensity of the spectral signal due to zenith angle variations converting the observed line signal into the corresponding zenit intensity. I will use the equation

$$F(z=0) = F\sqrt{1 - \left[\frac{R}{R+h}\right]^2 \frac{\mathrm{AM}^2 - 1}{\mathrm{AM}}} \tag{4.10}$$

where F is the signal from the line, R is the radius of the Earth and h the height of the airglow emission layer (see Table 2.1 at page 13). I used the approximation, $\mathrm{AM} \simeq 1/\cos z$, which is valid at low zenit distances. In the computation of the EW I used the corrected signal $F(z=0)$ instead of the original one. The code implemented is the following

```
C=1
#correct for zenital emission
if int(line) == 5577: #[OI]
    C = 1/np.sqrt(1-(6371/(6371+90))**2*(1-1/AM**2.))
if int(line) == 6300 or 6364: #[OI]
    C = 1/np.sqrt(1-(6371/(6371+275))**2*(1-1/AM**2.))
if int(line) == 5890 or 5896: #Na D
    C = 1/np.sqrt(1-(6371/(6371+92))**2*(1-1/AM**2.))
```

4.3.6 Data export

I export the new information about the continuum profile and the lines' EW into a new file. I decided to save in the same object the bidimensional sky spectrum, the EWs values and the profile of the continuum, each in a dedicated partition of the file. Data of the bidimensional spectrum is copied from the input file to the principal partition of the new one. The second partition of the output file contains a table with the wavelength of each line, the estimated EW, its error and a flag to specify whether the line is isolated or belong to a blended group. Information about the computation epoch, unit of measurement and blended lines selection criteria are saved in the relative header section. On the last partition of the output file is contained a table with the estimated unidimensional spectrum of the continuum, i.e. a table with wavelengths and the corresponding estimated continuum flux. The code to implement such features is the following:

```
#save as a new .FITS file
if FITS_lines is True:
    #save new FIT file with with EW in a partition
    table_hdu = fits.BinTableHDU.from_columns(
        [fits.Column(name = 'line', array = lines_raw, format = 'E'),
        fits.Column(name = 'EWs', array = EW_array, format = 'E'),
        fits.Column(name = 'EW_error', array = EW_error, format = 'E'),
        fits.Column(name = 'IsIsolated', array = close_lines, format = 'L' )])

    now = datetime.now()
    now_str = now.strftime("%Y-%m-%d %H:%M:%S")

    hdul.append(table_hdu)
    t_hdr = hdul[1].header
    t_hdr.set('UNITS', 'Angstrom')
```

```python
    t_hdr.set('EWTIME', now_str, 'Time of EW computation')
    t_hdr.set('LINERES', now_str, 'Min dist btw lines, in DELTA units')

    #save the continuum in a new partition too
    table_hdu = fits.BinTableHDU.from_columns(
        [fits.Column(name = 'LAMBDA', array = LAMBDA, format = 'E'),
         fits.Column(name = 'brightness', array = final_cont, format = 'E')])
    hdul.append(table_hdu)

    #save the .FITS file
    file_new = file[:-12]+'.l.fits'
    hdul.writeto(file_new, overwrite=True)
```

As shown above, to distinguish the new files from the previous version, this time i appeded the `.l.` suffix.

Chapter 5

Analysis and results

Here I report the results of my analysis on the spectra. The steps described below are rather easy and repetitive and mainly consist of plotting quantities, so I decided to include the relative code only in a few limited cases, where it can significantly improve the comprehension of the procedure I used.

5.1 Photometric sky brightness

A first preliminary test on the data results consists of calculating the brightness of the sky in the standard photometric system. The resulting values allow us to understand whether the flux calibration of the data was accurate enough.

5.1.1 Photometric conversion

In the Johnson photometric systems the energy flux through a band is computed as the mean of flux F_λ, throughout the transmission filter $T(\lambda)$, i.e.

$$\bar{F}_\lambda = \frac{\int_\lambda F_\lambda T(\lambda)\mathrm{d}\lambda}{\int_\lambda T(\lambda)\mathrm{d}\lambda} \tag{5.1}$$

We can pass to zenith magnitudes by using the Pogson law

$$\mu_\lambda = -2.5\log\left(\bar{F}_\lambda\right) - \mathrm{ZP}\left(\bar{F}_\lambda\right) + 2.5\log A + K \cdot \mathrm{AM} \tag{5.2}$$

where μ_λ is expressed in mag/arcsec^2 units, ZP is the zero-point value of the adopted photometric system, and A is the area of the sky from which the spectrum is taken. The last term, with AM the air mass, is added to compensate for the vertical luminosity profile of the sky.

The Johnson photometric system is defined such that the star Vega (α Lyr) has $V = 0.03\,\mathrm{mag}$ and all the color indices equal to zero. Known the mean spectra emission of Vega in the observing band $\bar{f}_{\lambda,\mathrm{Vega}}$, the zero-point value for the Johnson system is

$$\mathrm{ZP} = 2.5\log\left(\bar{F}_{\lambda,\mathrm{Vega}}\right) \tag{5.3}$$

Sky brightness zenital distribution. In polluted sites like Asiago the most impacting source of background light is the diffused radiation from artificial sources. The angular distribution of these sources is difficult if not even impossible to be properly modeled.

A standard way of proceeding is to implement an empirical calibration between the photometric magnitude correction and the observing air mass. This is done by measuring the sky brightness from the same field at different air masses and observe how it changes. From that analysis it can be derived the calibration coefficient K of equation (5.2), in units of mag/air mass.

In the case of Asiago observatory, I used the calibration obtained by prof. S. Ortolani in 2012 using the Schmidt telescope at Mount Ekar Observatory in Asiago (*Ortolani*, private communication). The calibration coefficient obtained and used in this work is $K = 0.3\,\mathrm{mag/airmass}$.

The area in the sky.   The lights that concur to the spectrum is selected by the width of the slit and vertically by the height of the spectrum on the detector (excluded eventual over-scan or unused regions). Horizontal extension of the light beam is equal to the size of the slit (in mm) multiplied by the angular scale of the telescope (arcsec/mm). Particular attention should be paid to the definition of the vertical extension. In my case I computed the flux as the average value of each wavelength, i.e. the resulting output values refer to the average flux per pixel. In that case vertical extension correspond to a single pixel, which can be converted in angular units using the scale on the detector (measured in arcsec/px). The total area used to compute the brightness is

$$A[\text{arcesc}^2] = \left(\frac{s[\text{μm}]}{1000.} c_{\text{tel}}[\text{arcsec/mm}] \right) (1\,[\text{px}] \cdot c_{\text{CCD}}[\text{arcsec/px}]) \tag{5.4}$$

Photometric bands.   As discussed above, due to calibration uncertainties, I ignored the spectral emission at wavelengths lower than 4000 Å. As shown in Figure 5.1, this limit is very close to the maximum of the B photometric filter, that cannot be used in the work. Similarly, in the red domain spectra typically range up to about 8000 Å, i.e. still in the tail of the R filter transmission range. Also the red filter may provide biased results and will not be used. Then the only filter totally compatible with those spectra is
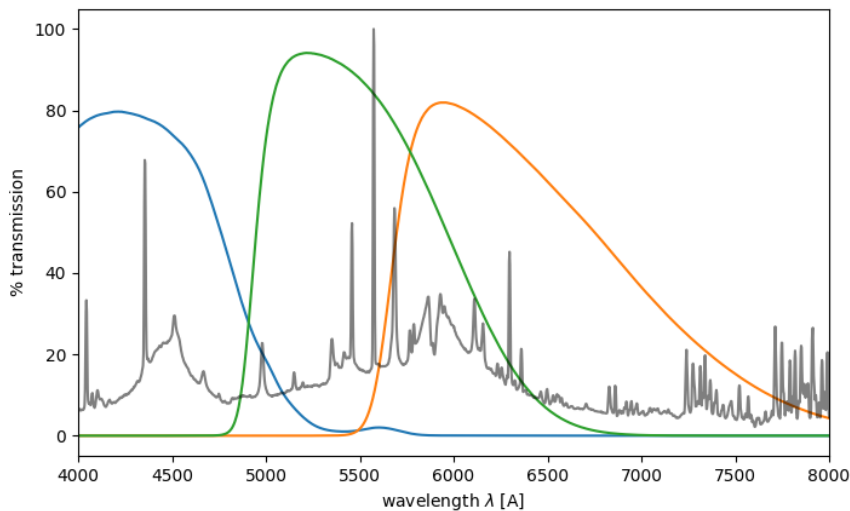

Figure 5.1: B, V and R photometric band transmission curves. An example spectra has been superimposed for reference. B and R sensitivity intervals span outside the spectral range so they cannot be used.

the V one.

5.1.2   Estimated V-band brightness

The results.   Using the procedure described above I can compute the estimated night sky brightness in Asiago from the spectral measurements. The overall trend is reported in Figure 5.2. From the statistical point of view, the Pearson correlation coefficient of the data is $\rho = -0.13$ from which I conclude no significant trends are present. From the data and the precision available, I can conclude the sky brightness in the V band from 2006 to 2021 ranged in the interval $V = 19.80 \pm 0.46\,\text{mag/arcsec}^2$.

Discussion.   Figure 5.2 tells us that the flux measurement obtained with this method is not very precise. Most of the photometric measures span in an interval of about $1\,\text{mag/arcsec}^2$, which correspond to a variation in the intrinsic flux of a factor 2.5.

Such an uncertainty is directly related to the uncertainty in the flux calibration in the original spectra. In spectroscopy, in fact, performing an accurate flux calibration is typically very challenging and the results may not always be optimal.

Another factor that can affect the total sky brightness are the sky conditions and in particular the presence of clouds or veils that can reflect back toward the ground upward artificial illumination. Another
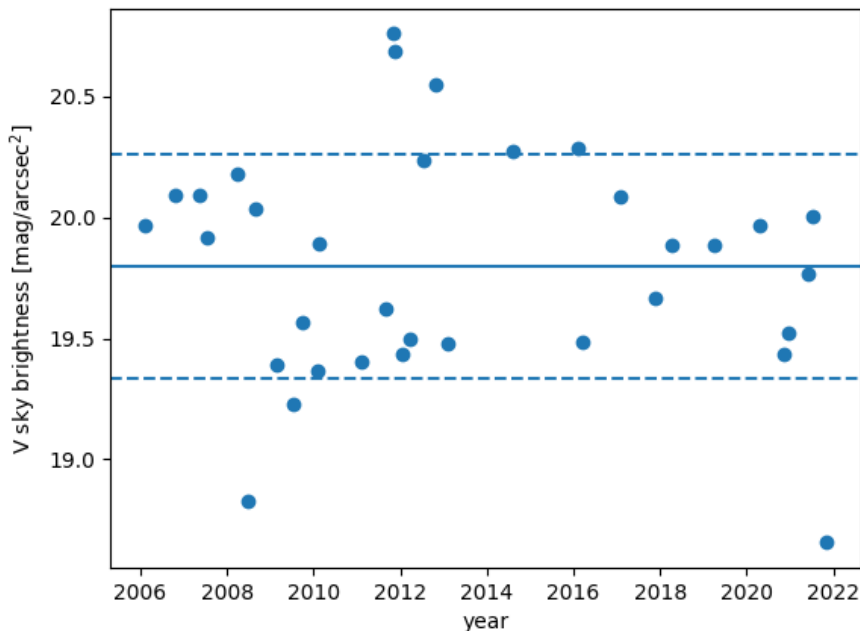
Figure 5.2: Estimation of the sky brightness in the V band from spectroscopic observations in Asiago. Average and $\pm 1\sigma$ lines are also shown. No general trend can be spotted.

phenomenon that occurs with partially covered skies is an increase of the atmospheric extinction, that can be measured for example as a dimming of the airglow emission. In Figure 5.3 is shown the emerging relation between the total brightness in the V band and the EW estimated for the [OI] atmospheric lines (for the details in their calculation see 4.3.4 and 4.3.5). As expected in the brightest skies atmospheric lines are systematically brighter. This suggests that part of the high dispersion in the brightness measurement is due to the presence of cloud coverage.

Regardless of the source, the high dispersion in the flux measurements prevents me from relying on "absolute" flux measurements on these data. For the rest of the spectroscopic I must focus on relative or normalized quantities and study the evolution of the *shape* of the spectra instead of considering absolute trends. In practice I have to find some indicators for the emission lines and the continuum, that are invariant for scale changes.

5.2 Line analysis

Here is reported the analysis on the evolution of the EW of some lines of interest in the night sky spectrum.

5.2.1 The measured lines

I focused only on a restricted number of the lines of Table 4.2. The selected lines matched the following criteria:

- Choose lines produced by all the main emission processes, i.e. take lines, from natural airglow and sodium and mercury lines. Lines produced by more than one mechanism at the same time, like the NaD doublet, are excluded.

- Choose isolated bright lines, when possible. Lines must be selected to obtain the best fit possible in the largest number of spectra. Interesting transitions such as the faint airglow $\lambda5199$ NI line are excluded since the line profile can be fitted correctly only in a couple of spectra.

- Choose unblended lines, when possible, i.e. exclude those bright lines that are the result of the overlap of lines of species from uncorrelated sources. For example I excluded the bright line at 4667 Å as it is the sum of Na, Hg and Sc transitions, totally blended with each other.
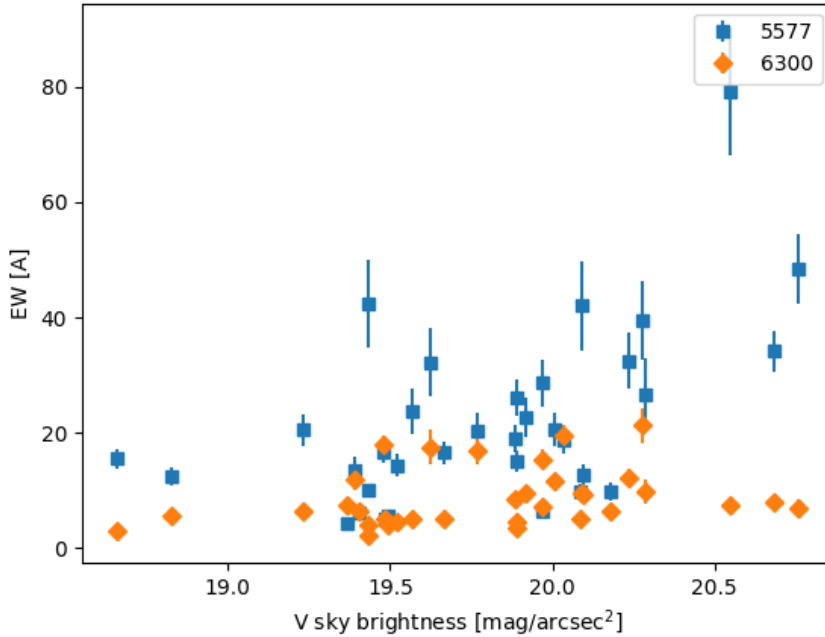
Figure 5.3: Sky brightness in the V band as a function of the EW of [OI] atmospheric lines. The line intensity seems to be correlated with the sky darkness, suggesting that the presence of thin cloud layers can be in part responsible for the high dispersion in the brightness measurements.

In Table 5.1 is reported the final list of the lines selected for the fit. Each group of lines has been selected to trace a single specific source.

source	wavelength (Å)	origin
Hg lamps	4046.56	HgI
	4358.34	HgI
	5354.03	HgI
Na lamps	4978.51, 4982.81	NaI
	5148.84, 5153.40	NaI
	6154.23, 6160.30	NaI
airglow	5577.34	[OI]
	6300.30	[OI]

Table 5.1: List of the fitted lines and their origin mechanism. Note due to the low spectral resolution Na doublets are considered a single line.

5.2.2   Evolution of the EW

The results.   In Figures 5.4, 5.5 and 5.6 are reported the EWs of lines from mercury-vapor lamps, sodium-vapor lamps and airglow respectively as a function of the observing epoch, expressed in years. I applied the linear regression method to estimate the rate of decrease of the EWs. Numerical results of the linear fits are reported in Table 5.1.

Comments and discussion.   I can list the main results from the analysis in the two following points:

- Concerning natural emissions the dispersion on the brightest 5577 Å presents very dispersed results. Among the possible causes the most likely is the fact that this bright line is partially blended with other nearby lines such as NaI ($\lambda\lambda 5682, 5688$) and HgI ($\lambda 5676$ and other minor ScI lines
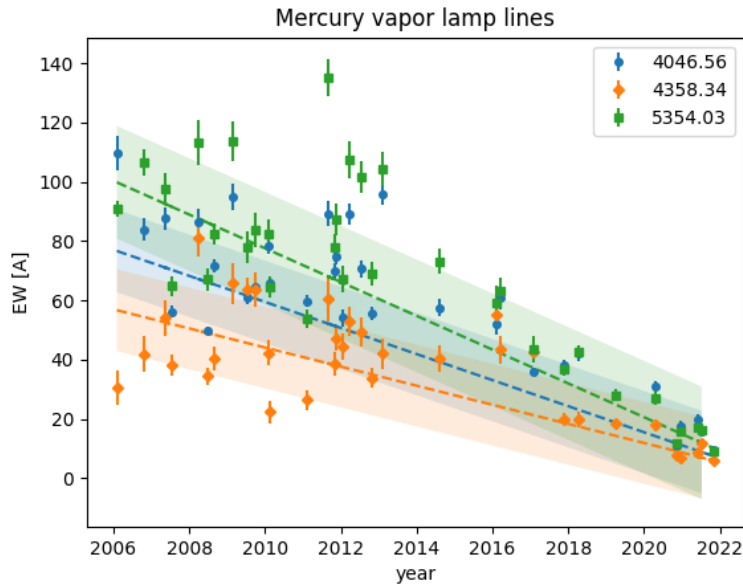
Figure 5.4: Evolution of the EWs of tree HgI transitions produced by mercury vapors lamps. Dashed lines represent the linear trend, colored bands are the $\pm 1\sigma$ confidence regions.
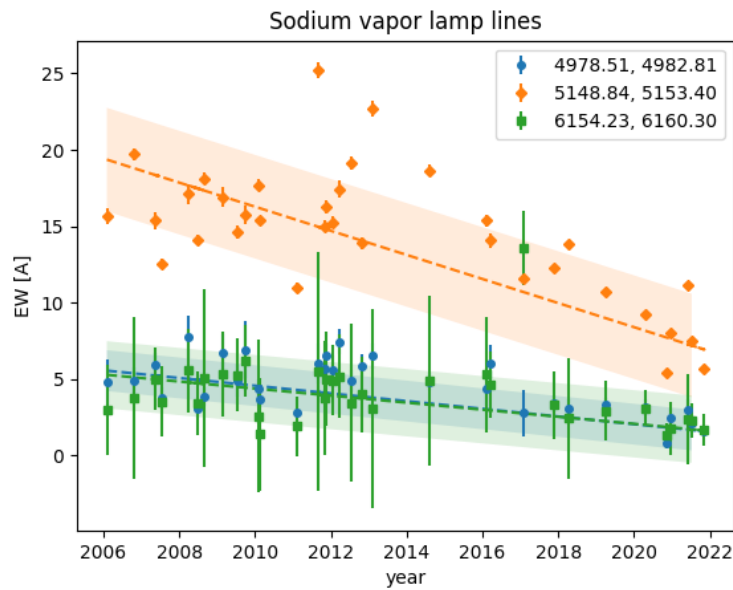

Figure 5.5: Evolution of the EWs of tree NaI transitions produced by sodium vapor lamps. Dashed lines represent the linear trend, colored bands are the $\pm 1\sigma$ confidence regions.

not resolvable); for a higher resolution spectrum and its comparison with my actual data, see Appendix A. Moreover, the continuum underlying the 5577 Å emission is not perfectly reliable since it contains several broad emission lines whose tails may partially contribute to the signal in the nearby $5610 - 5620$ Å sampling interval, slightly biasing the estimation of the continuum in the $5200 - 5800$ Å interval. Unfortunately, due to the distribution of the spectral features it is necessary to sample the continuum in such a region, even if the sampled data is not optimal.

- Artificial sources present a clear anti-correlation between lines EW and observation epoch. In the case of the [OI] airglow transitions the low correlation coefficient and the flat distribution of the points in the plots in Figure 5.6 suggest that airglow emission did not systematically changed in the last 15 years, but rather varied on short period timescales due to external environmental factors.
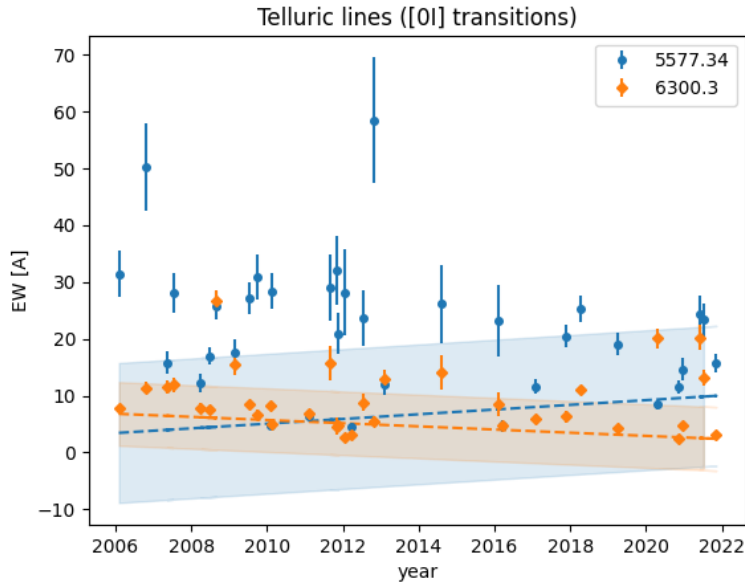
Figure 5.6: Evolution of the EWs of two [OI] airglow transitions. Dashed lines represent the linear trend, colored bands are the $\pm 1\sigma$ confidence regions.

source	wavelength [Å]	Pearson coefficient	rate of decrease [Å/yr]	total decrease (ΔEW/EW)	relative dispersion[a]
Hg lamps	4046.56	−0.85	−4.39	88%	31%
	4358.34	−0.69	−3.22	88%	42%
	5354.03	−0.82	−5.69	88%	33%
Na lamps	4978.51, 4982.81	−0.63	−0.25	70%	36%
	5148.84, 5153.40	−0.66	−0.79	63%	25%
	6154.23, 6160.30	−0.21	−0.23	67%	62%
airglow	5577.34	−0.22	+0.41	-	189%
	6300.30	−0.11	−0.28	-	118%

[a] Expressed as the ratio between the fit dispersion and the average best fit value.

Table 5.2: Statistical properties of the fitted lines. Due to the low correlation coefficient, the nearly flat trend and the high measurement dispersion I did not compute the total change in the EWs of airglow lines which would not be statistically relevant and possibly misleading. Moreover, from the physical point of view, no net trend is expected in the atmospheric lines.

Among the known and measurable factors that affect airglow intensity I remark the solar activity, see Appendix B.

- Both Hg and Na emission got drastically reduced between 2006 and 2021. Impact of Na lines decreased on average of 67% while Hg lines even 88%! The two different rates can be explained with the fact that mercury-vapor lamps started disappearing already in the 90s and now few remaining ones are being rapidly replaced with new technologies. The same process is stated occurring for the sodium-vapor in the last decade, so the replacement of these lamps is in an earlier phase.

5.3   Continuum analysis

The high uncertainty in the flux measurement of the original spectra do not allow us to study the absolute evolution continuum in the years, as discussed above (5.1.2). To overcome this issue I focused on the relative changes occurring in spectra over the time, i.e. the changes in the shape of the continuum.

5.3.1 Continuum relevance estimation

Estimation of the continuum impact

Since the flux calibration was uncertain (see 5.1), to quantify the relevance of the continuum in a given interval range $\Delta\lambda$ I used an indicator analogous to the EW used for spectral lines, which is invariant for flux scaling. I define the normalized flux C of the continuum in the interval $\Delta\lambda$ as

$$C = \frac{\int_{\Delta\lambda} F(\lambda)\mathrm{d}\lambda - F_0}{F_0 L} \tag{5.5}$$

where F is the spectral flux and F_0 is a normalization constant, that represents the level that the spectrum would have if the measured feature would not be there; L is the width of the considered band $\Delta\lambda$, and is used to compare different bands with different widths. Since in my case I am measuring the entity of light pollution, then F_0 represents the spectral flux that would be recorded without any artificial light while F is the original spectrum, where the contribution of the emission lines has been removed. In Figure 5.7 are reported the quantities described above in the case of my test frame.
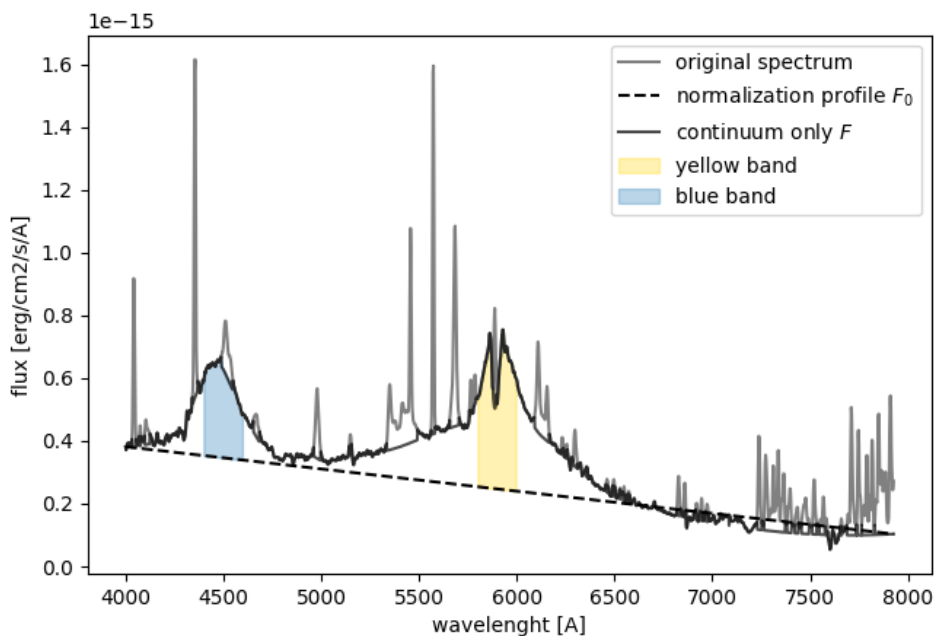

Figure 5.7: Example of continuum measurement on the test frame. Flux in the two bands is measured starting from the normalization profile F_0 (the dashed line).

The continuum F.   To correctly compute the impact of the continuum in a given band I have to remove automatically from the original signal the flux of the emission lines. Such lines can be highlighted by subtracting from the original signal the estimation of the continuum obtained from the initial spectrum analysis (see 4.3.3). The lines can be identified as those values of the residual signal that exceed a given threshold. After some tests, the best cutoff value proved to be the 70-th percentile of the residual signal. Residuals that exceeded this value were masked and the corresponding original signal replaced with the smooth continuum estimation. To be clearer I present a piece of pseudo-code that could make the operations described above.

```
res = spec-cont              #residuals
cut = np.percentile(res,70)  #cut threshold
cutted = res <= cut          #filter the signal
res[~cutted] = 0             #mask higher values
spec_noline = cont+res       #the cleaned signal
```

The normalization profile F_0. I approximated the normalization spectral profile (i.e. spectrum without the LP contribution) as a linear profile that connects the two extremes of the available spectrum. For values below 4200 Å and above 7500 Å spectra are not expected to be affected by particular emissions of artificial sources, as discussed in 3.2.2; tre profile F_0 should not significantly differ from the signal of the spectrum if we could remove the artificial sources.

Choice of the bands

I want to measure the flux index C of the continuum produced by t, HPS and LED lamps, whose spectra are reported in Figures 3.5 and 3.6 at page 21. These are the main two sources of artificial continuum since they are the most diffuse and pollutant types of lamps, at least around Asiago.

After some tests I found that the wavelength interval most sensitive to changes in the intensity of the blue peak of the LED lights is the interval $4400 - 4600$ Å. Similarly, the impact of HPS lamp spectrum is estimated from the analysis of its peak emission region, centered in the Na D doublet; the interval range I used is $5800 - 6000$ Å. The intervals and the spectral features they are measuring are shown in Figure 5.7.

Continuum uncertainty

I estimate the uncertainty in the indicator C by considering both the uncertainties on the spectrum, caused by the intrinsic noise, and the uncertainty on the determination of the normalization profile F_0. As approximate estimator of the flux measure error I used

$$\sigma_C = \frac{\sigma_{F_0} + \sigma_F}{L} \tag{5.6}$$

where with σ I represent the uncertainty of each profile.

Normalization profile uncertainty. Let denote with A and B the two extreme points of each spectrum, where the emission lines have been removed. The analytical equation for the normalization profile is

$$F_0(\lambda) = F_0(\lambda_A) + \frac{F_0(\lambda_A) - F_0(\lambda_B)}{\lambda_A - \lambda_B}(\lambda - \lambda_A) \tag{5.7}$$

I wonder how the shape of F_0 changes due to the noise fluctuations in the signal measured in A and B. Let σ_S be the noise amplitude, assumed constant over all the spectral range. Noise fluctuations of amplitude σ_S will provide some estimations for F_0 between the two extreme values

$$
\begin{aligned}
F_{0,\max} &= F_0(\lambda_A) + \sigma_S + \frac{F_0(\lambda_A) - F_0(\lambda_B) + 2\sigma_S}{\lambda_A - \lambda_B}(\lambda - \lambda_A) \\
F_{0,\min} &= F_0(\lambda_A) - \sigma_S + \frac{F_0(\lambda_A) - F_0(\lambda_B) - 2\sigma_S}{\lambda_A - \lambda_B}(\lambda - \lambda_A)
\end{aligned}
\tag{5.8}
$$

I approximate the uncertainty on the profile in the spectral range $\Delta\lambda$ centered at wavelength $\hat{\lambda}$ as the semi-dispersion between the two extreme values, i.e.

$$\sigma_{F_0} = \frac{F_{0,\max} - F_{0,\min}}{2} = \sigma + 2\frac{(\hat{\lambda} - \lambda_A)}{(\lambda_A - \lambda_B)}\sigma \tag{5.9}$$

Noise of the spectral profile. The same spectral noise that makes the determination of the normalization profile uncertain, affects also the computation of the integrated flux in the considered wavelength interval. I estimate the noise amplitude in the observing band $\Delta\lambda$ as the standard deviation of the residual profile, after the removal of the smooth continuum and the emission lines. If σ_λ represents such standard deviation in the observing band, then the total uncertainty on the measure of C is

$$\sigma_C = \frac{\sigma_S + (1 + m_\lambda) + \sigma_\lambda}{L} \tag{5.10}$$

where I grouped the constant terms into the variable $m_\lambda = 2(\hat{\lambda} - \lambda_A)/(\lambda_A - \lambda_B)$ to improve the readability.
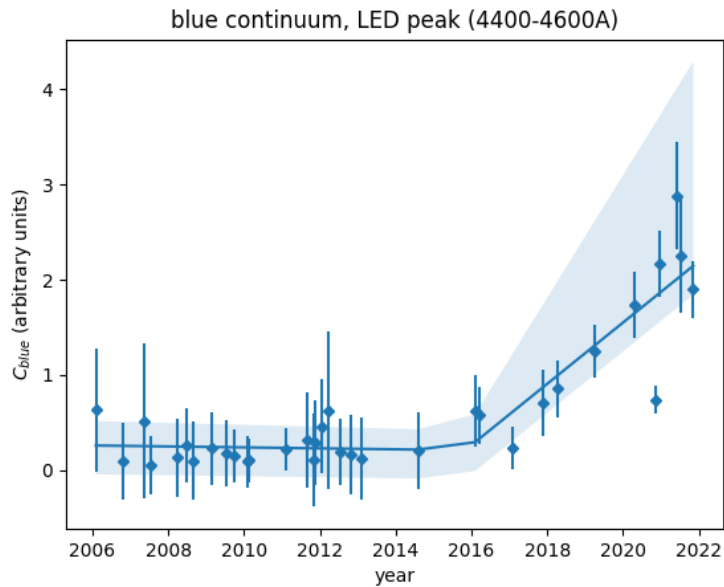
Figure 5.8: Evolution of the continuum intensity in the blue domain, between 4400 and 4600 Å in correspondence of the peak of LED lamps. The general trend can be divided into two periods: before 2016 continuum in this band is very low and constant with the time, while after 2016 we observe a rapid constant increase. Dashed lines represent the linear trend, colored bands are the $\pm 1\sigma$ confidence regions.
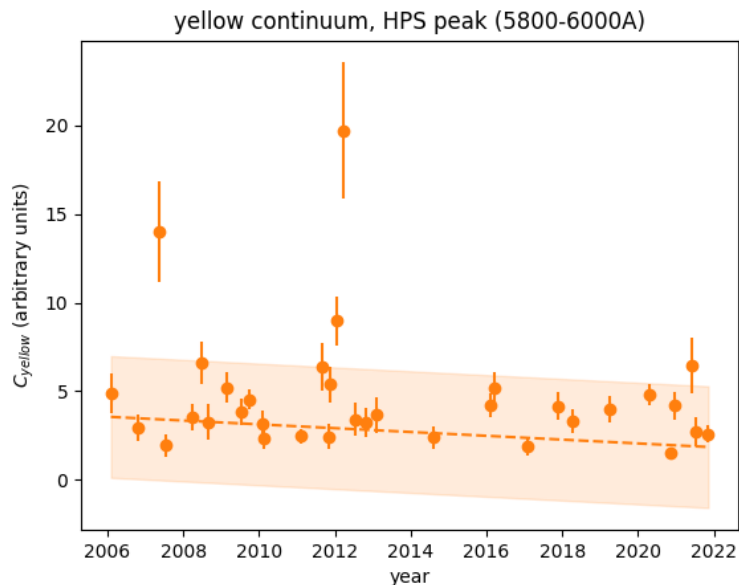

Figure 5.9: Evolution of the continuum intensity in the yellow domain, between 5800 and 6000 Å in correspondence of the peak of HPS lamps. A weak descending trend is observed. Dashed lines represent the linear trend, colored bands are the $\pm 1\sigma$ confidence regions.

5.3.2   Results

Figures 5.8 and 5.9 represent the evolution of the spectrum in correspondence of the blue and yellow bands from 2006 to 2021. Over the data I fitted some linear trends to obtain a synthetic indicator for the evolution of the spectra. The main results of the linear trend are reported in Table 5.3.

Blue continuum.   The region of the sky spectrum in the wavelength range between 4400 and 4600 Å is affected only by the natural sky bkg and eventually the presence of LED pollution. I decided to fit the

wavelength range [Å]	band	Pearson coefficient	total increase	relative dispersion[a]
4400 − 4600	blue (total)	+0.78	202%	49%
	blue (< 2016)	−0.07	−69%	71%
	blue (≥ 2016)	+0.82	207%	34%
5800 − 6000	yellow	−0.18	−47%	124%

[a] Expressed as the ratio between the fit dispersion and the average best fit value.

Table 5.3: Statistical properties of the continuum trends. The trend of the luminosity in the blue band has been splitted into two to better represent the data, reported in Figure 5.8. This choice is grounded on the fact LED lamps, the main sources of the blue band, were introduced only in the last decade.

data with a broken line, since the observations clearly showed two different behaviors: a nearly flat trend before roughly the 2016 and a steady increase after that year. Since 2016, emission in the considered band has doubled (+207%). This change in the trend can be explained with the introduction and diffusion of LED illumination in the last decade.

Yellow continuum. The region between 5800 and 6000 Å contains the peak emission of HPS lamps. Nevertheless, when we observe that the evolution of such continuum presents only a small and probably statistically not relevant decrease. This result seems in contradiction with the decrease observed from the emission lines of the HPS lamps, where a clear anti-correlation between EW and observing epoch is visible (refer to Table 5.2 and plots in Figure 5.5).

The most likely reason for this discrepancy is that LED emission is not limited to the primary blue peak but is partially re-distributed on longer wavelengths (recall Figure 3.6 at page 21) and will concur to the total luminosity observed in the yellow band. In the following pages I present a qualitative discussion of this hypothesis.

5.3.3 Impact of LED and HPS lamps

Here below I try to check how to disentangle the contribution of HPS and LED lamps in the total luminosity of the continuum in the yellow band; I wonder if the missing decrease in luminosity can be the result the increase of LED lights that compensate for the decrease of old HPS lamps.

Model LED and HPS contributions. I sketch a model of the emission in the $5800 − 6000$ Å range by using the following assumptions:

- The luminosity C_{blue} in the blue band is given by LED light only, i.e. I write $C_{\text{blue}} = C_{1,\text{LED}}$ where C is the continuum intensity indicator described above and in particular $C_{1,\text{LED}}$ denotes the intensity of the LED primary (blue) peak continuum emission.

- The luminosity in the yellow band is given by the sum of the HPS and LED contribution. I write $C_{\text{yellow}} = C_{\text{HPS}} + C_{2,\text{LED}}$ where $C_{2,\text{LED}}$ denotes the secondary peak of LED lamps.

- I estimate the unknown contribution of the secondary LED peak as a fraction k of the primary one, i.e. $C_{2,\text{LED}} = k \cdot C_{1,\text{LED}}$.

- I estimate the unknown contribution of HPS lamps in the yellow band as a fraction c of the (average) EW of emission lines originating from those lamps. I write $C_{\text{HPS}} = c \cdot \text{EW}_{\text{HPS}}$.

- Since both $C_{1,\text{LED}}$ and EW_{HPS} has been directly measured, I can model the ratio between the indicators C in the yellow and blue line as follows:

$$\frac{C_{\text{yellow}}}{C_{\text{blue}}} = \frac{C_{\text{HPS}} + C_{2,\text{LED}}}{C_{1,\text{LED}}} = \frac{c \cdot \text{EW}_{\text{HPS}} + k \cdot C_{1,\text{LED}}}{C_{1,\text{LED}}} = \frac{\text{EW}_{\text{HPS}}}{C_{1,\text{LED}}} \cdot c + k \tag{5.11}$$

Comparison with observed data. In Figure 5.10 I compare the modeled behavior of the ratio $C_{\text{yellow}}/C_{\text{blue}}$ with the actual data. The model (orange dashed line) fits the data with a precision comparable with a simple linear regression (dashed gray). Uncertainties on the data, in particular on the

least recent spectra, are really high and the results not statistically solid; due to such high error bars the model, as well as the linear regression, are poorly constrained.

If we assume the model of equation (5.11) is correct, then the best fit curve is characterized by $k = 0.75$, which means that the normalized flux of LED lights in the yellow band is the 75% of the one in the blue band, around its primary peak. This shows how the impact of LED lights is not limited to the bluer wavelengths only, but it affects a very large portion of the visible spectrum.
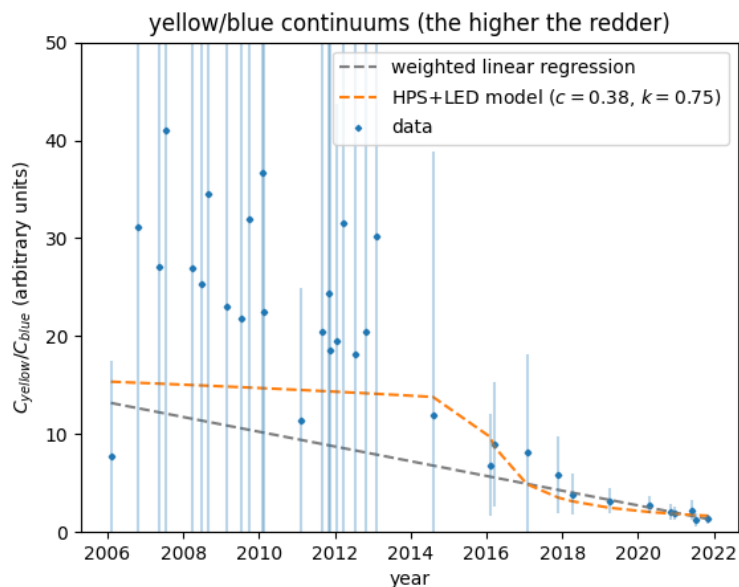

Figure 5.10: The ratio between the continuum intensity in the yellow and blue bands. The model of LED+HPS combined emission (dashed orange line) provides predictions similar to a simple weighted linear regression (green dashed line). The very high uncertainties on the data do not allow us to make definitive conclusions.

Chapter 6

Conclusions

6.1 Results of the work

In my work I confirmed that spectral observations from Asiago are significantly limited by the pollution due to artificial lights. The spectral analysis of the night background allow me to quantify the impact of the different LP sources and their evolution in the last 15 years. My quantitative analysis allowed me to confirm and measure some well expected trends in the night sky condition due to artificial pollution.

From 2006 to 2021 the of emission lines from the mercury vapor lamps (mainly HgI, ScI and ScII transitions) decreased by 88%. This means that in the last 15 years the light contribution of these lamps has nearly decimated. This drastic reduction was expected since mercury vapor-based lamps are a rather old and outdated technology and the few last remaining, when reaching the end of their life cycle are replaced with new LED systems. Moreover these lamps are very pollutant and their usage was progressively restricted in very specific situations.

Concerning sodium vapor-based illumination systems, from 2006 it was observed a decrease of about 67%, at least observing the associated spectral emission lines. Such slower decrease with respect to mercury-based lamps is due to the fact LPS and HPS lamps are a more recent technology, and their natural replacement is at an earlier stage; moreover, they do not have special restrictions like their predecessor. The decrease observed on the Na emission lines is not associated with a decrease in the luminosity in the bands where the continuum emission is produced. According to my work, it is possible that the green-orange domain of the HPS lamps was replaced by the emission of LED lights.

Finally in my work I observed a very fast increase in the usage of LED lamps, directly measurable through the integrated continuum emission of their primary peak, in the blue domain of the visible spectrum. Starting from 2016 emission in the blue band $(4400 - 4600\,\text{Å})$ saw an increase of 207%, while before that year the trend was apparently constant. Also this behavior was expected: LEDs were introduced in northern Italy only in the last decade and before 2016 in the blue band we do not expect any artificial continuum emission. After their introduction, LED rapidly spread as being used to replace old obsolete mercury-based lamps as well as the low-efficiency sodium-based ones.

In my analysis, I estimated that the LED emission in the yellow-orange domain (precisely in the range $5800 - 6000\,\text{Å}$) corresponds to up to 75% of the blue peak emission. As mentioned earlier, LED lamps are replacing the continuum emission of HPS lamps in the green-red visible spectrum; considering also their primary emission in the blue spectrum, we realize that LED is extremely pollutant in the whole visible spectrum.

6.2 Future perspectives

I develop the data reduction pipeline for this work in the most general and flexible way possible. My software is potentially able to analyze at least all the spectra taken with the $1.22\,\text{m}$ Galileo Telescope, virtually being able to provide a huge amount of information. Having more data may allow us to provide more solid estimations for the temporal evolution of the analyzed spectral features. Moreover, with a larger dataset it would be possible to sample and find correlations between the spectral features and other parameters such as the observation direction or the sky conditions, instead of limiting to the observation epoch only.

The eventual natural follow-up of this work is thus to analyze a larger sample of spectra to improve the reliability of the results and extend the analysis to a larger parameter space.

The heavy automation of my software also allows another possible employment: it may be used as a diagnostic tool for a real time quantification of the quality of the sky during an observation session. A practical example can be monitoring the intensity of artificially produced emission lines, that may change during the night following the sky conditions. If we revert the argument, it can be possible to retrieve the impact of changing sky conditions (haze or cloud formation, changes in temperature, pressure or humidity) on spectroscopic observations.

Another interesting followup of this work may be the systematic comparison between integrated brightness measurements obtained from spectral observations and the measurements obtained from the SQM sensor installed at the nearby Mount Ekar Observatory, Asiago, Italy. The comparison of two independent measurements would be useful to check and cross-validate the data collected from with the two techniques.

Appendix A

Asiago high resolution sky spectrum

In Figure A.1 I report the comparison between a high and low resolution spectra of the night sky from Asiago, taken with the 1.22 m Galileo Telescope and the Boller & Chievens spectrograph. The low resolution spectrum is analogous to the ones used in this work and has been obtained using a grating with 300 gr/mm; the high resolution spectrum was obtained with the 1200 gr/mm grating instead. Both spectra and the Figure are taken and provided by prof. Ciroi.

From a visual analysis it is clear how the original sky signal is smoothed in the low resolution spectrum. Many bright lines are dimmed in the peak value and broadened. In this way many close bright lines are blended together, making the estimation of the line widths more uncertain. Also the signal of the continuum in the low resolution spectrum is blended with the brightest emission lines, significantly altering the original spectral energy distribution. Due to the smoothing effect, many faint lines are not even detectable in the low resolution spectrum.
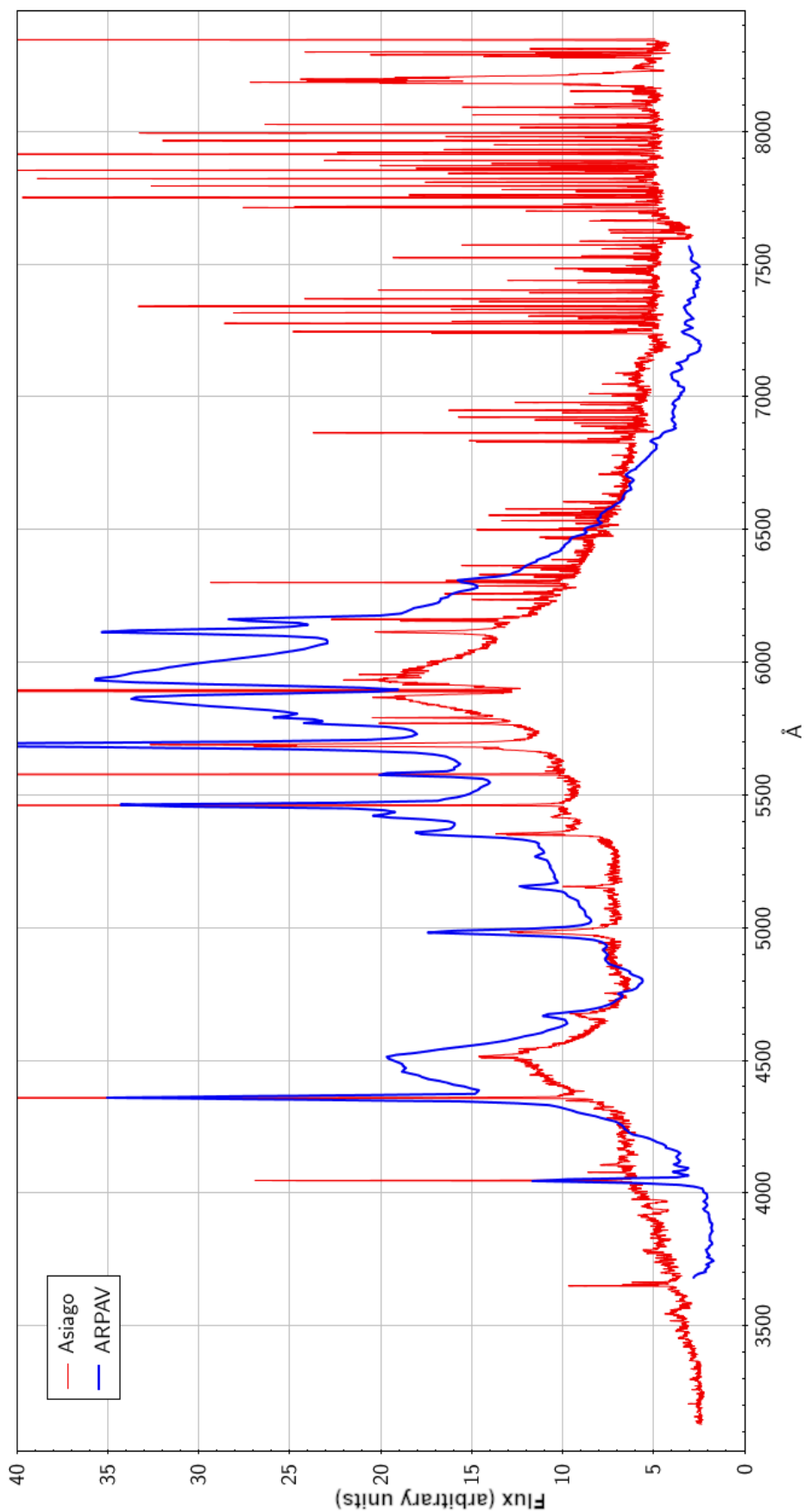
Figure A.1: A high resolution spectrum taken at Asiago (red) compared to a low resolution one (blue), analogous to the one used for this work. On low resolution spectra many features are blended into each other. Credits: S. Ciroi, private communication.

Appendix B

Airglow emission and solar activity

As discussed in 2.2, the airglow emission is affected by several factors, among which the variations of the solar activity. I can test whether the high dispersion in the measurements of the EW is related to the variations of the solar flux.

As a proxy for the solar activity I used the integrated flux from the emission of the radio line at 10.7 cm, provided by the National Oceanic and Atmospheric Administration (NOAA) agency. In Figure B.1 I report the solar activity within the time period of when my spectra has been taken.
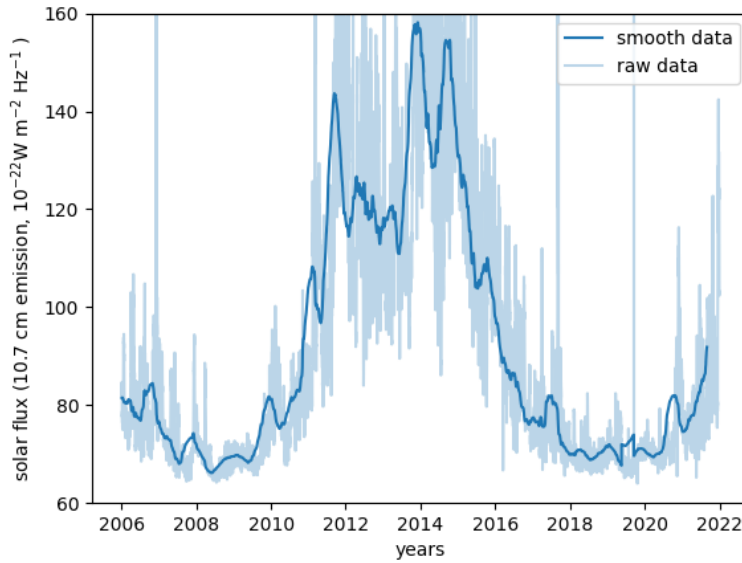

Figure B.1: 10.7 cm radio line flux according to NOAA recordings. To improve readability I also plotted a smoothed profile obtained with a rolling average of window 365 days on the data.

In Figure B.2 is taken the ratio between the EW of the two fitted [OI] lines and the solar solar activity at the observation time. Although the general trend seems quite constant, i.e. line EW seems proportional to the solar activity, the results present a very high dispersion. The relative dispersion of the data (computed as the ratio between standard deviation and average value) is respectively 120 and 128% i.e. the uncertainty is of the same order of magnitude of the measurements themselves.

To sum up, the intensity of atmospheric lines can significantly vary in time due to several factors. As shown here above, part of the EW dispersion is due to the changes in the solar activity. Another relevant factor, as discussed in 4.3.5, is the observing zenith distance. Finally in 5.1.2 I showed also how the presence of clouds and veils in the sky during the observation can produce higher levels of atmospheric extinction. Identifying and compensating for all these factors is very difficult if not even not possible with the data available, considering also the difficulties in a precise estimation of the widths of the lines, due to the low spectroscopic resolution and flux measurement uncertainties.
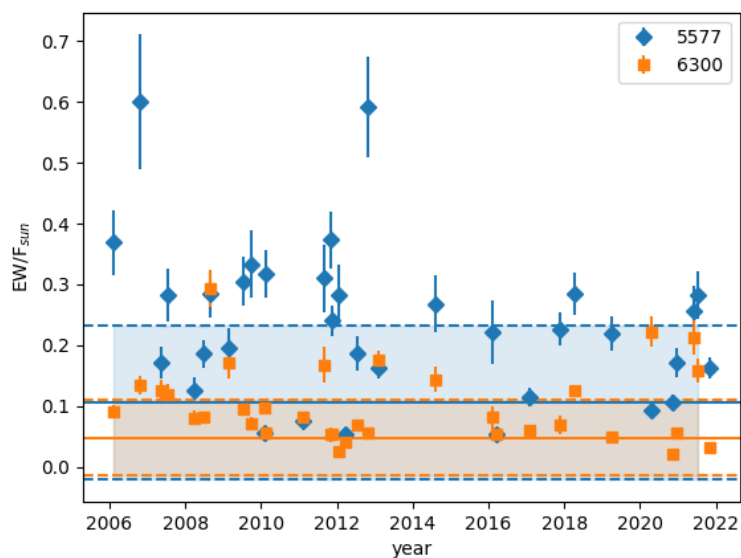
Figure B.2: Ratio between [OI] lines EW and the solar flux from the 10.7 cm radio band. Data are rather dispersed but look overall constant, proving a plausible correlation between solar activity and airglow line intensity. Dashed lines represent the linear trend, colored bands are the $\pm 1\sigma$ confidence regions.

Bibliography

[1] Astropy Collaboration. Astropy: A community Python package for astronomy. *Astronomy and Astrophysics*, 558:A33, Oct. 2013.

[2] F. C. Bertiau, E. de Graeve, and P. J. Treanor. The artificial night-sky illumination in Italy. *Vatican Observatory Publications*, 1:159–179, Jan. 1973.

[3] P. Cinzano. Inquinamento luminoso e protezione del cielo notturno [light pollution and protection of the night sky]. *Istituto Veneto di Scienze*, 1997.

[4] P. Cinzano. The propagation of light pollution in diffusely urbanised areas. *arXiv preprint astro-ph/9811293*, 1998.

[5] P. Cinzano. Disentangling artificial sky brightness from single sources in diffusely urbanized areas. *Mem. Societá Astronomica Italiana*, 71:113, Jan. 2000.

[6] P. Cinzano. The growth of light pollution in north-eastern italy from 1960 to 1995. *Memorie della Società astronomica italiana*, 71:159, 2000.

[7] P. Cinzano. Night sky photometry with sky quality meter. *ISTIL Int. Rep*, 9(1), 2005.

[8] C. Cottarelli, D. Bonata, F. Falchi, R. Furgoni, and C. Valdes. Illuminazione pubblica: spendiamo troppo [public illumination: we spend too much]. `https://osservatoriocpi.unicatt.it/cpi-archivio-studi-e-analisi-illuminazione-pubblica-spendiamo-troppo`, 2018. [Online; accessed 4-August-2022].

[9] R. H. Eather. Latitudinal distribution of auroral and airglow emissions: The 'soft'auroral zone. *Journal of Geophysical Research*, 74(1):153–158, 1969.

[10] F. Falchi, P. Cinzano, D. Duriscoe, C. Kyba, C. D. Elvidge, K. Baugh, B. A. Portnov, N. A. Rybnikova, and R. Furgoni. The new world atlas of artificial night sky brightness. *Science advances*, 2(6):e1600377, 2016.

[11] R. Falchi, T. Furgoni, T. A. Gallaway, N. A. Rybnikova, B. A. Portnov, K. Baugh, P. Cinzano, and C. D. Elvidge. Light pollution in usa and europe: The good, the bad and the ugly. *Journal of Environmental Management*, 248:109227, 2019.

[12] A. Frey, W. Hofmann, D. Lemke, and C. Thum. Photometry of the zodiacal light with the balloon-borne telescope thisbe. *Astronomy and Astrophysics*, 36:447–454, 1974.

[13] R. H. Garstang. Model for artificial night-sky illumination. *Publications of the Astronomical Society of the Pacific*, 98:364, mar 1986.

[14] A. Hänel, T. Posch, S. J. Ribas, M. Aubé, D. Duriscoe, A. Jechow, Z. Kollath, D. E. Lolkema, C. Moore, N. Schmidt, et al. Measuring night sky brightness: methods and challenges. *Journal of Quantitative Spectroscopy and Radiative Transfer*, 205:278–290, 2018.

[15] M. Hippke, T. J. David, G. D. Mulders, and R. Heller. Wōtan: Comprehensive Time-series Detrending in Python. *Astronomical Journal*, 158(4):143, Oct 2019.

[16] K. Krisciunas and B. E. Schaefer. A model of the brightness of moonlight. *Publications of the Astronomical Society of the Pacific*, 103(667):1033, 1991.

[17] C. Leinert, S. Bowyer, L. K. Haikala, M. S. Hanner, M. G. Hauser, A. C. Levasseur-Regourd, I. Mann, K. Mattila, W. T. Reach, W. Schlosser, et al. The 1997 reference of diffuse night sky brightness. *Astronomy and Astrophysics Supplement Series*, 127(1):1–99, 1998.

[18] Noll, S., Kausch, W., Barden, M., Jones, A. M., Szyszka, C., Kimeswenger, S., and Vinther, J. An atmospheric radiation model for cerro paranal - i. the optical spectral range. *A&A*, 543:A92, 2012.

[19] S. Ortolani and A. Bertolo. Checking the light pollution sources at Asiago Astrophysical Observatory from photometric and spectroscopic observations. Results from a unique experiment. In *IAU General Assembly*, volume 29, page 2252956, Aug. 2015.

[20] J. D. Ponz, R. W. Thompson, and J. R. Munoz. The fits image extension. *Astronomy and Astrophysics Supplement Series*, 105:53–55, 1994.

[21] S. F. Sánchez, J. Aceituno, U. Thiele, D. Pérez-Ramírez, and J. Alves. The night sky at the calar alto observatory. *Publications of the Astronomical Society of the Pacific*, 119(860):1186, 2007.

[22] SciPy 1.0 Contributors. SciPy 1.0: Fundamental Algorithms for Scientific Computing in Python. *Nature Methods*, 17:261–272, 2020.

[23] T. G. Slanger, P. C. Cosby, D. E. Osterbrock, R. P. S. Stone, and A. A. Misch. The high-resolution light-polluted night-sky spectrum at mount hamilton, california1. *Publications of the Astronomical Society of the Pacific*, 115(809):869, 2003.

[24] H. Tüg. Vertical extinction on la silla. *ESO Messenger*, 11:7–8, 1977.

[25] M. F. Walker. The effects of urban lighting on the brightness of the night sky. *Publications of the Astronomical Society of the Pacific*, 89:405, jun 1977.

[26] J.-C. Zhang, Z. Fan, J.-Z. Yan, Y. B. Kumar, H.-B. Li, D.-Y. Gao, and X.-J. Jiang. The night sky spectrum of xinglong observatory: Changes from 2004 to 2015. *Publications of the Astronomical Society of the Pacific*, 128(968):105004, 2016.

Web resources

- Image archive. ESO.
  `https://www.eso.org/public/images/`

- Gateway to Astronaut Photography of Earth. NASA.
  `https://eol.jsc.nasa.gov/SearchPhotos/photo.pl?mission=ISS043&roll=E&frame=143486`

- Wikimedia Commons.
  `https://commons.wikimedia.org/wiki/Main_Page`

- Desmos Graphing Calculator.
  `https://www.desmos.com/calculator/`

- Illuminazione pubblica spendiamo troppo. Osservatorio CPI [8].
  `https://osservatoriocpi.unicatt.it/cpi-archivio-studi-e-analisi-illuminazione-pubblica-spendiamo-troppo`

- Light pollution map.
  `https://www.lightpollutionmap.info`

- Archivio immagini. CieloBuio.
  `https://www.cielobuio.org/cielobuio/arc-imm.htm`

- codatomrc/tesi. GitHub.
  `https://github.com/codatomrc/tesi`

- The Python Standard Library.
  `https://docs.python.org/3/library/index.html`

- SciPy User Guide.
  `https://docs.scipy.org/doc/scipy/tutorial/index.html#user-guide`

- wotan. PyPI.
  `https://pypi.org/project/wotan/`

- Astropy Documentation.
  `https://docs.astropy.org/en/stable/`

- NOAA Solar Radio Flux at 10.7 cm, Time Series.
  `https://lasp.colorado.edu/lisird/data/noaa_radio_flux/`

List of acronym

- bkg = background
- CCD = Charge-Coupled Device
- EW = Equivalent width
- FITS = Flexible Image Transport System
- FWHM = Full Width at Half Maximum
- HPS = High-Pressure Sodium [lamps]
- IAU = International Astronomical Union
- LP = Light Pollution
- LPS = Low-Pressure Sodium [lamps]
- LED = Light Emission Diode
- NOAA = National Oceanic and Atmospheric Administration
- SNR = Signal-to-Noise Ratio
- SQM = Sky Quality Meter
- UV = Ultra Violet
- ZL = Zodiacal Light